Biophysical Journal
Article

Biophysical Society

Multiscale imaging and quantitative analysis of plasma membrane protein-cortical actin interplay

Aparajita Dasgupta,[1] Huong-Tra Ngo,[1] Deryl Tschoerner,[1] Nicolas Touret,[2] Bruno da Rocha-Azevedo,[1] and Khuloud Jaqaman[1,3,*]

[1]Department of Biophysics, University of Texas Southwestern Medical Center, Dallas, Texas; [2]Department of Biochemistry, University of Alberta, Edmonton, Alberta, Canada; and [3]Lyda Hill Department of Bioinformatics, University of Texas Southwestern Medical Center, Dallas, Texas

ABSTRACT The spatiotemporal organization of cell surface receptors is important for cell signaling. Cortical actin (CA), the subset of the actin cytoskeleton subjacent to the plasma membrane (PM), plays a large role in cell surface receptor organization. However, this has been shown largely through actin perturbation experiments, which raise concerns of nonspecific effects and preclude quantification of actin architecture and dynamics under unperturbed conditions. These limitations make it challenging to predict how changes in CA properties can affect receptor organization. To derive direct relationships between the architecture and dynamics of CA and the spatiotemporal organization of PM proteins, including cell surface receptors, we developed a multiscale imaging and computational analysis framework based on the integration of single-molecule imaging (SMI) of PM proteins and fluorescent speckle microscopy (FSM) of CA (combined: SMI-FSM) in the same live cell. SMI-FSM revealed differential relationships between PM proteins and CA based on the PM proteins' actin binding ability, diffusion type, and local CA density. Combining SMI-FSM with subcellular region analysis revealed differences in CA dynamics that were predictive of differences in PM protein mobility near ruffly cell edges versus closer to the cell center. SMI-FSM also highlighted the complexity of cell-wide actin perturbation, where we found that global changes in actin properties caused by perturbation were not necessarily reflected in the CA properties near PM proteins, and that the changes in PM protein properties upon perturbation varied based on the local CA environment. Given the widespread use of SMI as a method to study the spatiotemporal organization of PM proteins and the versatility of SMI-FSM, we expect it to be widely applicable to enable future investigation of the influence of CA architecture and dynamics on different PM proteins, especially in the context of actin-dependent cellular processes.

SIGNIFICANCE Plasma membrane protein organization, an important factor for shaping cellular behaviors, is influenced by cortical actin, the subset of the actin cytoskeleton near the plasma membrane. It is challenging to directly and quantitatively probe this influence. Here, we developed an approach that combines single-molecule imaging, fluorescent speckle microscopy, and computational statistical analysis to characterize and quantitatively correlate the spatiotemporal organization of plasma membrane proteins and cortical actin. We derived quantitative relationships that could predict differences in protein mobility, even between subcellular regions, based on differences in cortical actin dynamics. We expect this approach to be widely used to shed new light on the influence of cortical actin on plasma membrane components, especially in the context of actin-dependent processes.

INTRODUCTION

The spatiotemporal organization of cell surface receptors plays an important role in cell signaling (1–4). It modulates ligand binding (5,6), receptor interactions (7–9), and recruitment of downstream effectors (1,3,10). Multiple factors affect cell surface receptor organization and function, including interactions with plasma membrane (PM) proteins and lipids (11–13), the extracellular matrix (14,15), and the cell cortex (16–18). Cortical actin (CA), a major constituent of the cortex, exerts both direct influence on PM proteins, and indirect influence through its effect on lipids (19–21). Its influence is in part described by the picket-fence model, where the filamentous CA meshwork acts as a barrier to the diffusion of PM proteins and lipids (15,21–23). However, CA filaments also form dynamic structures that may influence PM protein (and lipid) movement and clustering

Submitted January 27, 2023, and accepted for publication August 8, 2023.

*Correspondence: khuloud.jaqaman@utsouthwestern.edu

Aparajita Dasgupta and Huong-Tra Ngo contributed equally to this work.

Editor: Maria F. Garcia-Parajo.

https://doi.org/10.1016/j.bpj.2023.08.007

(24–28). At the same time, cell surface receptor signaling can regulate CA remodeling (29,30). Thus, studying the dynamic organization of and interplay between CA and PM proteins is critical for a comprehensive understanding of cell surface receptor signaling.

A limiting factor for studying the interplay between CA and the spatiotemporal organization of the PM is that the CA meshwork is too dense to simultaneously resolve its architecture and dynamics with conventional light microscopy (31). Therefore, insights into the role of the cortex in PM organization have come largely from perturbation-based studies (22,28,32). Single-molecule (SM) imaging (SMI) and tracking of several PM molecules have shown that perturbing actin leads to faster diffusion of these molecules, or to an increase in their freely moving population, in line with CA acting as a barrier (33,34). However, perturbations preclude the quantification of CA architecture and dynamics under *unperturbed* conditions. They also compromise PM integrity and cell health.

To complement/circumvent perturbation experiments, a few previous studies employed simultaneous imaging of PM molecules and CA to directly visualize the correlation between CA and the spatiotemporal organization of PM molecules. By combining SMI of PM proteins with conventional imaging of actin, it was observed that B cell receptors were less mobile in actin-rich regions versus actin-poor regions (33) or that FCεRI receptors were excluded from crossing into actin-rich regions (35). To probe CA at higher resolution, one study employed a combination of super-resolution radial fluctuations, fluorescence correlation spectroscopy, and number and brightness analysis (36). While actin disruption by latrunculin A (Lat A) altered the mobility of EGFR in this study, no direct correlation was found between the diffusion or clustering of EGFR and CA. The influence of actin on EGFR mobility was thus inferred to be indirect through the influence of actin on the PM overall (36). Meanwhile, Li et al. (23) used fluorescent magnetic nanoparticles to drag and image PM proteins across the PM, followed by super-resolution imaging of CA using dSTORM. They found that PM protein movement encountered resistance in areas with dense CA filaments. Yet, despite the co-imaging of PM proteins and CA, these studies provided mostly a static view of CA, thus limiting the characterization of CA dynamics.

To observe the spatiotemporal organization of PM proteins and, simultaneously, the architecture and dynamics of CA with high spatiotemporal resolution, we combined SMI of PM proteins with fluorescent speckle microscopy (FSM) of CA in live cells (combined: SMI-FSM). In FSM, actin monomers are labeled substoichiometrically, so that speckles are formed when several monomers come together due to actin polymerization. FSM allows quantitative characterization of CA architecture, turnover, and movement (37), and is well-suited to probe CA dynamics alongside the spatiotemporal organization of PM proteins (probed through SMI). Monitoring PM proteins and CA simultaneously is challenging, given their disparate spatial and temporal scales. To overcome these challenges, we designed a multiscale imaging scheme to monitor PM proteins and CA each at its relevant timescale and developed a computational analysis pipeline to parse the acquired data, explore the multidimensional data set of dynamic PM protein properties and associated CA properties, and derive quantitative relationships between the measured properties.

MATERIALS AND METHODS

Plasmids

Plasmid encoding CD36-fused at the N-terminus to HaloTag (Halo-CD36) was generated by PCR cloning the HaloTag coding sequence (primer details in Table S1, Integrated DNA Technologies) from pFN21K HaloTag CMV Flexi Vector (Promega, Madison, WI), followed by ligation in place of the mApple sequence in the mApple-CD36-C-10 vector (Addgene, Watertown, MA, plasmid no. 54874 (5)), using restriction enzymes *Age*I and *Bgl*II (New England Biolabs, Ipswich, MA). To generate Halo-TM-ABD (TM-ABD: chimeric protein consisting of the actin binding domain [ABD] of ezrin fused to the transmembrane domain of the folate receptor) and Halo-TM-ABD* (TM-ABD*: equivalent to TM-ABD but with the point mutation R579A in the ABD to eliminate actin binding), Halo-CD36 plasmid was linearized using restriction enzymes *Eco*RI and *Bgl*II (New England Biolabs) to release the CD36 fragment. TM-ABD or TM-ABD* fragments were then seamlessly cloned (Takara Bio, San Jose, CA) into the linearized HaloTag vector by PCR amplification (primers details in Table S1, Integrated DNA Technologies) from GFPTM-Ez-AFBD and GFPTM-Ez-AFBD*, respectively, with corresponding flanking homology. GFPTM-Ez-AFBD and GFPTM-Ez-AFBD* were a generous gift from Satyajit Mayor Lab (NCBS, India) (24). PLVXCMV100mNeonGreenActin, pSPAX2, and pMD2G plasmids were a generous gift from Gaudenz Danuser lab (UTSW, Dallas, TX) (38).

Cell lines and cell culture

Human telomerase-immortalized microvascular endothelial cells (MVECs) isolated from human foreskin (TIME [telomerase-immortalized microvascular endothelial] cells, ATCC, Manassas, VA), or TIME cells stably expressing mNeonGreen-Actin (TIME-mNGrActin; see description of cell line generation below), both at passage 16 or higher (unless indicated otherwise), were grown in ATCC's vascular cell basal medium supplemented with MVEC growth kit-VEGF and 12.5 μg/mL blasticidine (Sigma-Aldrich, St. Louis, MO, 203351) for 48 h at 37°C + 5% CO_2 until reaching 80–90% confluency. Then cells were passaged and plated on fibronectin-coated (10 μg/mL, MilliporeSigma, Burlington, MA), base/acid cleaned, 0.17 mm (no. 1.5) glass bottom dishes (14 mm glass diameter, MatTek, Ashland, MA) or 6 well plates for 18 h before experiments.

Generation of TIME-mNGrActin cell line

Lentiviral transduction was performed to generate TIME cells stably expressing mNeonGreen-tagged actin (TIME-mNGrActin). In brief, HEK293T cells (Danuser lab) were transfected using 3 μL/μg polyethylenimine (Sigma-Aldrich, 408727) with PLVX-mNeonGreenActin-CMV-100 (4 μg) along with VSV envelope vector pSPAX2 (2 μg) and viral packaging construct pMD2G (2 μg). PLVX-mNeonGreenActin-CMV-100 has the fluorescent fusion protein expressed from a truncated CMV promoter containing only the first 100 basepairs from the 5′ end of the CMV promoter (38). Viral media were harvested after 48 h, filtered (0.45 μm pore size), and mixed with 0.5 μL/mL dilution of polybrene (MilliporeSigma, TR-1003-G). To generate the TIME-mNGrActin cell line, TIME cells at 50% confluency were incubated

with viral medium mixed with polybrene for 72 h. Infected cells at the lower range of mNeonGreen-actin expression were enriched using fluorescence-activated cell sorting using a FACSAria system (Children's Research Institute Flow Cytometry Facility, UTSW, Dallas, TX).

Transient transfection

For experiments comparing CD36, TM-ABD, and TM-ABD*, and for the 200 nM Lat A treatment data set, TIME-mNGrActin cells (0.75 to 1×10^5 cells) were seeded on fibronectin-coated glass bottom dishes, and, after 18 h, were transiently transfected with Halo-CD36 (0.25 μg), Halo-TM-ABD (0.25 μg), or Halo-TM-ABD* (0.25 μg) using Transfex transfection reagent (ATCC, ACS-4005). Imaging experiments were performed 2 days after transfection. For experiments with cells plated for 4 h, TIME-mNGrActin cells (7.5×10^4 cells) were seeded in 6-well plates, and, after 18 h, were transiently transfected with Halo-CD36 (0.25 μg) using Transfex transfection reagent. On day 2 after transfection, 5×10^4 cells were seeded on fibronectin-coated glass bottomed dishes and imaged within 4 h. For all these cases, medium containing transfection complex was replaced with complete culture medium after 20 h of transfection. For experiments involving 30 nM Lat A treatment and the corresponding untreated cells, TIME-mNGrActin cells at 80–90% confluency were transiently transfected in suspension with Halo-CD36 (1 μg) using Universal Transfection Reagent (Sigma-Aldrich, T0956). Medium containing transfection complex was replaced with complete culture medium 6 h after transfection. Transfected cells were passaged the next day and 1×10^5 cells were seeded on fibronectin-coated glass bottom dishes. Imaging experiments were performed 2 to 3 days after transfection in this case.

Halo labeling for SMI

TIME-mNGrActin cells transfected with PM proteins as described above were incubated for 15 min in complete culture medium with 3 nM JF549-Halo ligand (experiments comparing CD36, TM-ABD, and TM-ABD*, and the 200 nM Lat A data set) or 15 nM JF549-Halo ligand (30 nM Lat A data set), 2–3 days post transfection. JF549-Halo was a generous gift from Dr. Luke Lavis, Janelia Research Campus, Ashburn, VA (39). For 4 h plating experiments, CD36 transfected TIME-mNGrActin cells were allowed to adhere for 3 h on fibronectin-coated glass coverslips, after which they were incubated with 3 nM JF-549-Halo ligand (~2 days post transfection). In all cases, incubation with dye was followed by three quick washes in sterile DPBS. Cells were then incubated for 15 min in dye-free complete culture medium. Incubations were at 37°C + 5% CO_2. Finally, cells were washed three times (5 min each) with wash buffer (HBSS +1 mM HEPES and 0.1% normal goat serum [NGS] for live cells). Cells were incubated in imaging buffer (OxyFluor 1%, glucose 0.45%, and Trolox 2 nM) to reduce photobleaching before and during imaging.

Drug treatments and perturbations

For cell fixation with paraformaldehyde (PFA), cells were incubated with a 4% PFA solution made in PBS (Electron Microscopy Sciences, Hatfield, PA, 15710) for 15 min at room temperature (RT) and then washed three times (5 min each) with wash buffer (HBSS + 0.1% NGS for fixed cells) before adding imaging buffer. For cell fixation with PFA + glutaraldehyde (glut), cells were incubated with a 4% PFA + 0.1% glut (Electron Microscopy Sciences, 16020) solution made in PBS, for 20 min at 4°C, in the dark. Freshly prepared quenching solution (0.1% NaBH4, Oakwood Chemical, Estill, SC, 042896) was added immediately after fixation and cells were incubated for 7 min. Samples were washed three times (5 min each) at RT with wash buffer. For Lat A treatment, TIME-mNGrActin cells expressing Halo-CD36 labeled with JF549-Halo ligand were incubated with 30 nM or 200 nM Lat A (Thermo Fisher Scientific, Waltham, MA, L12370), diluted in imaging buffer, at the microscope, as described in the following section.

Multiscale SMI-FSM data acquisition

For experiments comparing CD36, TM-ABD, and TM-ABD*, and for the 30 nM Lat A data set, TIME-mNGrActin cells expressing Halo-CD36, Halo-TM-ABD, or Halo-TM-ABD*, and labeled with Halo ligand, were imaged at 37°C using a total internal reflection fluorescence (TIRF) system (S-TIRF, Spectral Applied Research, via BioVision Technologies, Exton, PA) mounted on a Nikon Ti-E inverted microscope with Perfect Focus and a 60×/1.49 NA oil TIRF objective (Nikon Instruments, Melville, NY). The system was equipped with two Evolve EMCCD cameras (Photometrics, Tucson, AZ) for one-color or simultaneous two-color imaging, registered to within 1–3 pixels of each other. A custom 3× tube lens was employed to achieve an 89 nm × 89 nm pixel size in the recorded image. Illumination by a 561 nm diode pumped solid-state laser (Cobolt) and/or a 488 nm diode laser (Coherent) was achieved through an ILE laser merge module (Spectral Applied Research, Ontario, Canada), with 561 and 488 nm laser power of 13.2 and 3.65 mW, respectively, at the coverslip. The penetration depth was set to 80 nm via the Diskovery platform control (Spectral Applied Research). Single-bandpass emission filters, ET520/40 and ET605/52 (Chroma Technology, Bellows Falls, VT), and a dichroic to direct the emission beam to the two cameras (Chroma Technology, 565dcxr), were used in the emission path.

For the 4 h plating experiments, and for the 200 nM Lat A data set, TIME-mNGrActin cells expressing Halo-CD36, and labeled with Halo ligand, were imaged at 37°C using an Olympus IX83 TIRF microscope equipped with a Z-Drift Compensator and a UAPO 100×/1.49 NA oil-immersion TIRF objective (Olympus, Tokyo, Japan). The microscope was equipped with an iXon 888 1k × 1k EMCCD Camera (Andor; Oxford Instruments). With an additional 1.6× magnification in place, the pixel size in the recorded image was 81 nm × 81 nm. Using the Olympus CellSens software, excitation light of 491 and 561 nm from an Olympus CellTIRF-4Line laser system was directed to the sample by a TRF8001-OL3 Quad-band dichroic mirror. Laser powers at the coverslip were 4.9 and 9.1 mW for the 491 and 561 nm laser lines, respectively. The penetration depth was set to 80 nm via the cellSens software (Olympus). Emission beams of different wavelengths were collected using bandpass emission filters ET520/40m and ET605/52m (Chroma) and projected onto different sections of the camera chip by an OptoSplit III 3-channel image splitter (Cairn Research, Faversham, UK).

On either microscope, videos were acquired with MetaMorph (Molecular Devices, San Jose, CA) in the stream acquisition mode, with the two channels acquired simultaneously, using the trigger function to control illumination. The 561 channel was used for acquiring SMI videos. These were acquired at 10 Hz for 50 s (501 frames) or 90 s (901 frames). The 561 channel was triggered to remain open (i.e., continuous illumination) for the entire duration of the video. Simultaneously, the 488/491 channel was used for acquiring FSM videos. While the 488/491 channel was acquired also at 10 Hz (for the same number of frames as the 561 channel), the 488/491 channel was triggered to illuminate the sample only every 50th frame for 100 ms. Removing the "empty" 488/491 channel frames (those in the absence of 488/491 illumination) (using MetaMorph, post video recording), resulted in an FSM time lapse at 0.2 Hz for 11/19 FSM frames corresponding to the 501/901 SMI frames. All videos were acquired using an EM gain of 100. Temperature and humidity were maintained using an environment chamber (Okolab, Otaviano, Italy), maintaining cell viability for the duration of the experiments.

For the CD36, TM-ABD, and TM-ABD* data set, and the 4 h plating data set, multiple cells were acquired sequentially (for 50 s each) over ~40 min of imaging. For the 30 nM Lat A and its corresponding unperturbed data set, a single cell was selected from the dish and followed over time, where it was imaged for three instances of 1.5 min each, with an ~5 min resting interval between the imaging instances (for a total session time of ~25 min). In this case, Lat A was added to the sample at the microscope, after selecting a cell for imaging. The first imaging instance started almost immediately after Lat A addition. For the 200 nM Lat A

and its corresponding vehicle-control data set, one cell was recorded at the start of each imaging session, after which either imaging buffer alone or imaging buffer containing Lat A was added, and then multiple cells were acquired sequentially (for 50 s each) over ~30 min of imaging. For both, the 30 and 200 nM Lat A data sets, the time at which Lat A or vehicle was added was recorded and used to calculate the time post-perturbation.

Every SMI-FSM movie was preceded by a bright-field snapshot of the imaged cell region to visually check cell viability.

FSM of actin with and without fixation

TIME-mNGrActin cells were either left untreated (live) or fixed using PFA + glut (as described above). Both live and fixed cells were then imaged at 37°C using an Olympus IX83 TIRF microscope (described above). The penetration depth was set to 70 nm via the cellSens software (Olympus). Excitation light of 491 nm from an Olympus CellTIRF-4Line laser system was directed to the sample. Power was 2.31 mW at the coverslip. FSM videos were acquired at a frame rate of 0.2 Hz for 109 frames (9 min). This was equivalent to the FSM arm of the SMI-FSM data acquisition scheme described above, although with longer acquisition time.

Actin FSM + phalloidin imaging

TIME-mNGrActin cells plated on fibronectin-coated glass bottom dishes were fixed with 4% PFA (as described above). Following fixation, sample was incubated with Alexa Fluor 647 phalloidin (Thermo Fisher Scientific, A22287) at 1:20 dilution in blocking buffer (1% BSA, 5% NGS in wash buffer). After washing, cells were incubated in imaging buffer and imaged at 37°C using an Olympus IX83 TIRF microscope (described above). For excitation, light of 640 nm (0.2 mW at coverslip) and 491 nm (2.3 or 5.1 mW at coverslip) from an Olympus CellTIRF-4Line laser system was directed to the sample. The penetration depth was set to 100 nm via the cellSens software (Olympus). First, the 640 channel was imaged for an exposure time of 99 ms. Then, the 491 channel was used for acquiring FSM videos at 10 Hz for 5 frames. Fluorescence of each wavelength was collected, filtered with emission filters of ET520/40m and ET705/72m (Chroma Technology), and projected onto different sections of the camera chip by an OptoSplit III 3-channel image splitter (Cairn Research). Camera EM gain was set to 100 for all acquisitions.

Immunofluorescence imaging of endogenous CD36 and VEGFR2 expression

TIME cells plated for 20 h were washed once in wash buffer to remove the culture medium and then fixed with 4% PFA (as described above). After 3 washes, samples were blocked for 15 min in blocking buffer and then incubated with primary antibodies, against either CD36 (1:400, FA6-152, Abcam, Cambridge, UK, ab17044) or VEGFR2 (1:200, Abcam, ab9530) for 1 h at RT. After three washes, samples were incubated with Alexa Fluor 488-conjugated secondary antibodies (1:1000, Thermo Fisher Scientific) for 15 min at RT. Finally, after three subsequent washes, dishes were incubated with imaging buffer to reduce photobleaching. Immunofluorescence (IF) imaging was then performed using the S-TIRF microscope described above using a 488 nm laser power of 2.6 mW at the coverslip.

IF imaging and analysis of phospho-Src enrichment at CD36 spots

TIME cells, transiently transfected with Halo-CD36 for 2 days, were serum starved for 3 h. After 2 h of starvation, cells were labeled with 10 nM JF549-Halo ligand. The samples were then exposed to either 10 nM thrombospondin-1 (TSP-1) (R&D Systems, 3074-TH) or HBSS for 10 min at 37°C. After 10 min, the samples were washed with wash buffer and then fixed with PFA + glut (as described above) in the dark. Cells were then incubated for 7 min with freshly prepared quenching solution. Samples were then washed three times (5 min each) at RT with wash buffer, and then permeabilized using 0.1% Triton X-100. After three washes with wash buffer, samples were blocked for 15 min in blocking buffer and then incubated with Alexa Fluor-conjugated primary antibody against phospho-Src (Tyr419) (Thermo Fisher Scientific, 44-660G). Finally, after three subsequent washes, dishes were incubated with imaging buffer to reduce photobleaching. IF imaging was performed as describe above, using laser powers of 13.2 mW for the 561 channel (CD36) and 3.65 mW for the 488 channel (pSrc) at the coverslip. The two channels were imaged sequentially (561 followed by 488).

For the analysis of pSrc enrichment at CD36 spots from the acquired IF images, the centers of CD36 spots were determined using "point-source detection" in u-track (40,41) (https://github.com/DanuserLab/u-track). In the detection step, default parameter values were used, except for an α value of 0.01 for determining object detection significance by comparing the fitted amplitude with the local background noise distribution. A point spread function (PSF) sigma of 1.228 pixels was used. Enrichment analysis was carried out as described in the "Intensity enrichment analysis" section of (5). To compare the control and TSP-1 stimulated data sets to each other and to their randomizations, multiway analysis of variance with default linear model was performed (MATLAB function anovan()) followed by Tukey-Kramer post hoc analysis.

SM particle detection and tracking

SM tracks were constructed from the SMI streams using u-track (40) (version 2.2.1; https://github.com/DanuserLab/u-track). Detection was achieved using the "Gaussian mixture-model fitting" option. The SM detection and tracking parameters were optimized based on the performance diagnostics included in u-track and visual inspection of the results. The mean SM localization precision, as estimated during the Gaussian mixture-model fitting step (40), was 16–24 nm. Tables S2 and S3 list the detection and tracking parameters with nondefault values. The tracks output by u-track were then processed and refined to discard too short tracks (duration <10 time points) and tracks outside the cell mask, and to process merging and splitting events (Note S1; Fig. S1 *A*).

Quantitative FSM analysis and extraction of CA speckle properties

FSM time lapse sequences were analyzed using the Quantitative FSM (QFSM) software package (37), following the instructions in (42). In brief, first noise model calibration was performed to estimate spatial correlation in background noise (42) (step 1). Then cell masks were generated either within the QFSM package at the thresholding and mask refinement steps (steps 2 and 3) or manually (if thresholding failed). Then speckles were detected (step 4) and tracked (step 5) within the cell mask. The flow tracking step (step 6) was not utilized as the speckles in our movies did not exhibit collective flow. Polymerization/depolymerization events were tracked to generate kinetic maps (step 7; although not used for further analysis). QFSM parameters were optimized based on visual inspection of the results. Parameters with nondefault values are listed in Tables S4–S6. The speckle tracks output by QFSM software were then processed to calculate individual CA speckle properties (e.g., position, displacement, intensity, and lifetime) (Note S2; Fig. S1, *B* and *C*), and subsequently global speckle properties within the cell ROI mask (regardless of the vicinity of any SM; Note S3).

Multivariate regression analysis of SM tracklet and local speckle properties

Linear multivariate regression (MVRG) (using the MATLAB function mvregress()) was performed on an individual cell (movie) basis. SM

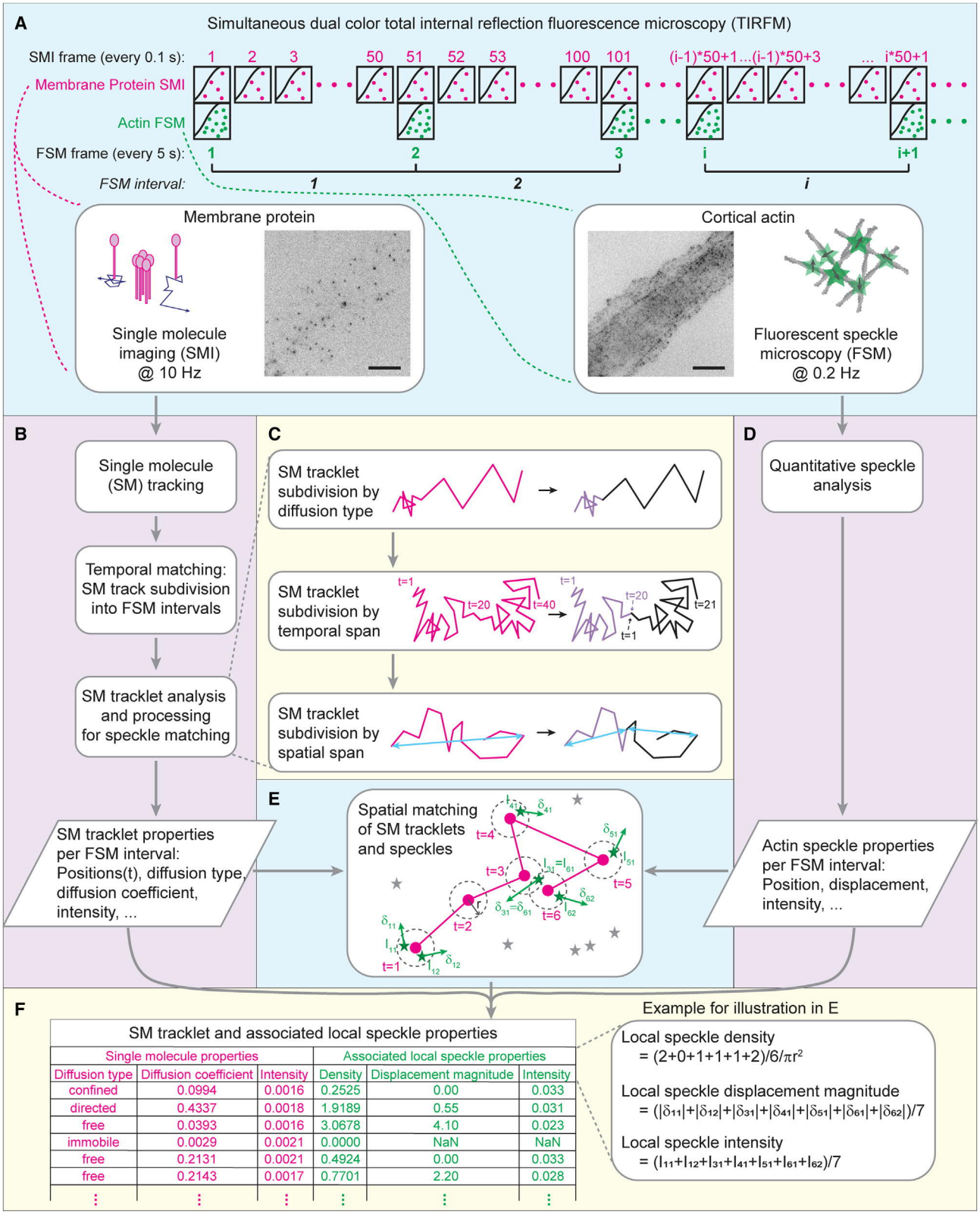

Single molecule properties			Associated local speckle properties		
Diffusion type	Diffusion coefficient	Intensity	Density	Displacement magnitude	Intensity
confined	0.0994	0.0016	0.2525	0.00	0.033
directed	0.4337	0.0018	1.9189	0.55	0.031
free	0.0393	0.0016	3.0678	4.10	0.023
immobile	0.0029	0.0021	0.0000	NaN	NaN
free	0.2131	0.0021	0.4924	0.00	0.033
free	0.2143	0.0017	0.7701	2.20	0.028

FIGURE 1 SMI-FSM yields dynamic properties of PM proteins and neighboring CA speckles. (*A*) SMI-FSM data acquisition schematic, showing the relationship between SMI and FSM frames. The 51 SMI frames from FSM frame *i* to FSM frame *i*+1 correspond to FSM interval *i*. Insets, example PM protein SMI (*left*) and CA FSM (*right*), with illustrations. Scale bar, 10 μm. (*B*) Major data processing steps of the SMI branch. (*C*) Substeps of the SM tracklet analysis and processing step. Magenta indicates a tracklet before processing; purple and black indicate tracklets after processing. t, tracklet time points;

(legend continued on next page)

tracklet properties were taken as the response ("dependent") variables and the associated local speckle properties were taken as the design matrix ("independent variables"). Each property was normalized by its sample mean and standard deviation before MVRG analysis. For any combination of SM tracklet and speckle properties, only complete datapoints (i.e., datapoints without any missing values for any of the properties of interest) were utilized. MVRG was performed only when there were at least 11 complete datapoints. To check multicollinearity in the design matrices (i.e., interdependence between the "independent variables"), the variance inflation factor was calculated for each performed MVRG (43).

MVRG yielded per-cell regression coefficients quantifying the extent of (mathematical) dependence of any SM tracklet property on the coanalyzed local speckle properties (one coefficient per SM tracklet-CA speckle property pair). The MVRG coefficients of the set of cells representing a particular experimental condition were then grouped for subsequent analysis of their significance and their comparison between experimental conditions. Upon grouping, outlier single-cell MVRG coefficients were identified using the generalized extreme Studentized deviate test, useful for detecting multiple outliers in a univariate data set that follows an approximately normal distribution (44) (MATLAB function isoutlier(data, 'gesd')).

Statistical tests for comparing SM or speckle properties or MVRG coefficients

To compare SM or speckle properties, or MVRG coefficients, between two experimental conditions, a two-sample *t*-test was performed (MATLAB function ttest2()). If more than two experimental conditions were compared, multiway analysis of variance with default linear model was performed (MATLAB function anovan()), followed by Tukey-Kramer post hoc analysis (MATLAB function multcompare()).

To compare SM or speckle properties, or MVRG coefficients, between the Free and Confined subsets of SM tracklets of an experimental condition, or between the Center and Edge regions of a cell, a paired-sample *t*-test was performed (MATLAB function ttest()). A paired-sample *t*-test was appropriate in this case as each measurement of the Free subset had a corresponding measurement of the Confined subset from the same cell, and similarly for the Center and Edge measurements.

To compare SM or speckle properties between two experimental conditions at a particular instance (30 nM Lat A data set) or time interval (200 nM Lat A data set), a two-sample *t*-test was performed. To compare between two experimental conditions across all instances/time intervals, the mean over all cells at each instance was calculated per condition, and then the two groups of per-instance means were compared using a paired *t*-test (paired by instance).

For all of the above tests, comparisons with p values ≤ 0.05, 0.01, or 0.001 were indicated in the figures using *, **, or ***, respectively, while comparisons with a p value > 0.05 were not marked (to reduce clutter).

Statistical tests for assessing the significance of MVRG coefficients

To determine whether there was a significant relationship between an SM tracklet property and an associated CA speckle property, a one-sample *t*-test was performed, with the null hypothesis that the single-cell MVRG coefficients followed a normal distribution with mean zero (MATLAB function ttest()). A relationship was considered significant if the *t*-test yielded a $p \leq 0.05$. To assist with visualizing these relationships, the MVRG coefficient plots were annotated with overhead triangle pictograms, where the triangle slopes represent the significance and sign of the MVRG coefficients. Nonsignificant MVRG coefficients were represented with rectangles.

As additional evidence for the significance of any identified SM tracklet-speckle property relationship (where the MVRG coefficient *t*-test yielded $p \leq 0.05$), we performed MVRG analysis after data set shuffling and calculated the fraction of shuffled data MVRG coefficients with a p value smaller than that of the real data MVRG coefficient (Table S7). Specifically, suppose we were performing MVRG using n SM properties and m speckle properties. To obtain the corresponding shuffled data MVRG coefficients, the pairing of the n SM tracklet properties and the m speckle properties was shuffled, while keeping the n SM properties together and the m speckle properties together. For each MVRG analysis, the shuffling analysis was performed 100 times. The fraction of p values from shuffled data smaller than significant p values from real data was 0–0.06, further supporting the significance of the identified relationships.

RESULTS AND DISCUSSION

Multiscale SMI-FSM of PM proteins and CA in live single cells

To develop and validate SMI-FSM, we generated a stable TIME cell line expressing mNeonGreen-actin from a truncated CMV promoter (TIME-mNGrActin cell line). The combination of a truncated CMV promoter and cell selection through FACS ensured low labeling of actin for FSM (Fig. 1 *A*, Video S1). mNeonGreen-actin speckles appeared throughout the imaged cell area in a manner that correlated with CA density probed via phalloidin staining (Fig. S2). Although fusing mNeonGreen to actin might interfere with the activity of formin actin nucleators (45), actin structures dependent on formin activity, such as filopodia and stress fibers, were well labeled in TIME-mNGrActin cells (Fig. S2 *A*). This suggested that mNeonGreen-actin speckles were largely a faithful reporter on actin structures at the probed spatiotemporal scales, consistent with previous studies using this construct (38).

We then transiently expressed in TIME-mNGrActin cells Halo-tagged versions of three model transmembrane proteins: TM-ABD (chimeric protein made of the ABD of ezrin fused to the transmembrane domain of the folate receptor), TM-ABD* (a mutated form of TM-ABD with the mutation R579A in ABD to inhibit binding to actin) (24,46), and the cell surface receptor CD36 (47) (Fig. S3 *A*). TM-ABD and TM-ABD* served as actin-binding and actin-nonbinding controls, respectively. CD36 was a particularly interesting model protein because, while previous studies have shown that the actin cytoskeleton is important for its mobility, clustering, and signaling at the PM in multiple cell types (5,7,48), it has no known direct interaction with actin.

cyan double arrows represent the spatial span of each tracklet. (*D*) Data processing in the FSM branch. (*E*) Illustration of spatial matching of SM tracklet (*magenta dots* and connecting lines) and neighboring speckles (*green stars*). Dashed circles, area for matching, with radius r. I_{tm}, intensity; δ_{tm}, displacement (vector) of speckle m matched to SM tracklet at time point t. Gray stars, speckles not matched to this SM tracklet. (*F*) Example table with SM tracklet and associated local speckle properties. Inset to right: calculation of local speckle properties, for illustration shown in (*E*). To see this figure in color, go online.

Rather, the influence of actin on CD36 is most likely indirect, through intermediate molecules (13,48,49). As such, the interplay between CD36 and CA is expected to be representative for many PM constituents, the majority of which are influenced by CA indirectly (16). Labeling of the Halo-tagged proteins with JF549-conjugated Halo ligand enabled SMI alongside FSM (Fig. 1 *A*; Video S2).

CD36 is expressed naturally in MVECs, where it initiates signaling that inhibits angiogenesis upon binding its ligand TSP-1 (47,50). However, for our experiments, we employed TIME-mNGrActin cells of passage 16 or higher, because, at these passages, TIME cells exhibited very little to no endogenous CD36 (Fig. S3 *B*; as is the case with higher-passage primary MVECs (5)), allowing us to work exclusively with the exogenous Halo-CD36. Halo-CD36 was able to trigger downstream signaling in response to stimulation by TSP-1 as expected, indicating that it was functional (Fig. S3 *C*) (5,50).

The first challenge of SMI-FSM was to maximize the information content of the experiments, given the fast dynamics of PM proteins and the slower dynamics of CA. To monitor PM proteins and CA each at its relevant timescale, we devised a multiscale data acquisition scheme where we performed SMI at a frame rate of 10 Hz (7,51) and simultaneously FSM at a frame rate of 0.2 Hz (52) (Fig. 1 *A*; see materials and methods). This allowed us to image for a long enough time period to capture CA dynamics (50–90 s) while minimizing fluorophore photobleaching and cell phototoxicity. We used TIRF microscopy for both, to focus on the bottom cell surface and the subjacent cortex. SMI videos were then analyzed using particle tracking (40) to obtain SM tracks of the imaged PM proteins (Video S3). At the same time, the associated FSM videos were analyzed using QFSM software (42) to detect and track the CA speckles (Video S4), from which various CA speckle properties were derived (Notes S2 and S3).

Integration of PM protein and neighboring CA speckle properties

The distinct timescales of SMI and FSM led to challenges in putting their data sets together to derive quantitative relationships between the properties of PM proteins and CA. To address these challenges, we developed a computational pipeline that bridged the timescale gap and linked SM tracks to their neighboring speckles in space and time (Fig. 1). The pipeline, which yielded a multidimensional data set of PM protein properties and associated CA speckle properties, consisted of the following steps.

Step 1. Temporal matching of SM tracks and speckles

With our imaging strategy, each FSM frame-to-frame interval spanned 51 SMI frames (FSM frame 1 = SMI frame 1, FSM frame 2 = SMI frame 51, etc.; Fig. 1 *A*). For temporal matching between SM tracks and speckles, we subdivided the SM tracks by the FSM intervals (Fig. 1 *B*). An average of 44% of SM tracks (range: 37–49% per movie) crossed FSM interval boundaries and were thus segmented into multiple tracklets. Henceforth, we will refer to the temporally matched SM trajectories, and any further subdivisions thereof, as SM tracklets.

Step 2. SM tracklet analysis and processing for spatial matching with speckles

In preparation for matching (the temporally matched) SM tracklets to CA speckles in space, we performed the following SM tracklet analyses and processing (Fig. 1 *C*). Our goal was to obtain a collection of SM tracklets such that each tracklet: 1) was as localized as possible in space to increase the accuracy of matching SM tracklets and CA speckles and 2) exhibited homogeneous diffusion properties to increase the sensitivity of our subsequent analysis of the coupling between SM behavior and neighboring CA speckle behavior. Note that SM track processing before this integration step already segmented tracks at merging and splitting events to avoid changes in clustering properties within each tracklet (Note S1).

Step 2a. We obtained the diffusion properties of SM tracklets using transient diffusion analysis (DC-MSS (53)). Transient diffusion analysis allowed us to segment an SM tracklet into multiple tracklets if a change in diffusion type was detected. An average of 1.7% of SM tracklets (range: 0.7–3.6% per movie) exhibited diffusion type switches. With this, each SM tracklet (after segmentation, if any) was characterized by its diffusion type (free, confined, immobile, directed) and diffusion coefficient. Note that DC-MSS requires trajectories to be at least 20 time points long; thus, tracklets with duration less than 20 time points remained unclassified and were not usable for any analyses utilizing SM tracklet diffusion properties.

Step 2b. After Step 2a, SM tracklets could have a duration between 10 time points (minimum duration retained; Note S1) and 51 time points (number of SMI frames within an FSM interval). To reduce the variability in tracklet duration, and thus the variability in the amount of information contained in each SM datapoint when analyzing the coupling between SM behavior and CA speckle behavior, we segmented tracklets lasting $\geq$40 time points (twice the minimum duration possible for diffusion analysis (53)) in half. Each half became a separate tracklet, and its diffusion properties (diffusion type and diffusion coefficient) were calculated. An average of 3.9% of SM tracklets (range: 1.9–7.0% per movie) from step 2a had a duration $\geq$40 time points.

Step 2c. Some SM tracklets, particularly those of fast-moving molecules, spanned a distance >3 μm. At such length scales, CA properties could vary spatially (54,55), and it would be meaningless to combine CA speckle properties along the tracklet for subsequent analysis steps. Thus, to obtain spatially localized tracklets, we segmented

SM tracklets spanning a distance >3 μm into shorter daughter tracklets, each spanning a distance <3 μm. The spatial span of an SM tracklet was defined as the maximum distance between any pair of positions along the tracklet. Any tracklet with a span between 3(m–1) μm and 3m μm (where m = 2, 3, …) was segmented into m daughter tracklets of roughly equal duration. Any resulting daughter tracklet with a spatial span >3 μm was subsequently segmented further, using the same procedure, until all tracklets in the final set had a spatial span $\leq$3 μm. An average of 3.7% of the tracklets (range: 1.0–5.6% per movie) from Step 2b spanned a distance >3 μm. Because all SM tracklets after step 2b had a duration <40 time points, daughter tracklets resulting from this step had a duration <20 time points and their diffusion properties could not be analyzed separately. Rather, the daughter tracklets from this step inherited the diffusion properties (diffusion type and diffusion coefficient) of the original SM tracklet from step 2b.

With these steps, we obtained the following properties for each SM tracklet:

- diffusion type
- diffusion coefficient
- SM spatial span
- SM intensity, defined as the mean particle intensity over the tracklet duration.

Step 3. Spatial matching of SM tracklets and CA speckles

For each SM tracklet in an FSM interval, we determined its neighboring speckles based on its positions at every time point and the speckle positions at the starting frame of the FSM interval (Fig. 1, *D* and *E*; Video S5). Specifically, speckles that were within a distance r of 3.5 pixels from any position within the SM tracklet were considered to be neighboring speckles. The radius r = 3.5 pixels primarily accounted for the registration shift between the two cameras (for the two channels) in our imaging setup (51).

Step 4. Calculation of local speckle properties around SM tracklets

After matching speckles to SM tracklets, we calculated the local speckle properties around each SM tracklet, as described in Note S4. With this, we obtained the following local speckle properties for each SM tracklet.

- Local speckle density. Co-imaging of CA speckles and phalloidin-stained actin demonstrated that local speckle density reflected local CA density (Fig. S2; Note S5).
- Local speckle displacement magnitude. Local speckle displacement represented network remodeling resulting from filament turnover and motor protein induced movement (56,57). There was no systematic actin flow in our experimental conditions.
- Local speckle intensity. Local speckle intensity represented the quantity of fluorescently labeled actin.

Through steps 1–4, we put together, for each SM tracklet, a list of its properties (step 2) and its local CA speckle properties (step 4) (Fig. 1 *F*). SM tracklets without any matched speckles (~20% of SM tracklets) had a speckle density of zero and no other associated speckle properties. We then compiled together the SM tracklet and associated local speckle properties from all FSM intervals of an individual cell. Outliers within each property were identified and removed (using the interquartile range method, also called Tukey's fences method (44), with thresholds that retained about 99% of the datapoints). Altogether, this provided us with a multidimensional data set of SM tracklet and associated local speckle properties to investigate their relationships in an explicit and quantitative manner.

The spatiotemporal organization of CD36, TM-ABD, and TM-ABD* reflects their actin-binding ability

Application of the analysis pipeline to SMI data of CD36, TM-ABD, and TM-ABD* revealed that ~60% of their tracklets diffused freely, ~30% exhibited subdiffusive behavior—consisting of ~20% confined and ~10% immobile—and ~10% exhibited directed diffusion (Fig. 2 *A*). The actin-binding control, TM-ABD, had a significantly lower/higher fraction of free/subdiffusive (confined and immobile) SM tracklets than the actin-nonbinding control, TM-ABD* (Fig. 2 *A*). CD36 exhibited intermediate behavior between the actin-binding and nonbinding controls. The diffusion coefficients per diffusion type (free or confined) of the three PM proteins were similar (Fig. 2 *B*). Our results for TM-ABD and TM-ABD* are consistent with previous studies, where it was observed that TM-ABD undergoes more tethering and/or slower diffusion than TM-ABD* (15,46). The intermediate behavior of CD36 suggests that its actin-binding ability is weaker and less direct than that of TM-ABD (which binds actin directly), but stronger and more specific than that of TM-ABD* (which has no specific interaction with actin). This is consistent with CD36 interacting with other molecules that themselves interact with actin (13,48,49).

Our analysis also shed light on the clustering of the imaged molecules (captured by their SM intensity) and its relation to their diffusion type. Here (and for most subsequent analyses), we focused on the free and confined SM tracklets, as they constituted the majority of tracklets. We found that confined CD36 tracklets had significantly higher intensities than free CD36 tracklets, while TM-ABD and TM-ABD* showed no difference in SM intensity between free and confined tracklets (Fig. 2 *C*). Note that the small—but significant—difference in intensity between free and confined CD36 tracklets (~4% difference) most likely reflects a substantially larger difference in their true clustering states, given the substoichiometric labeling

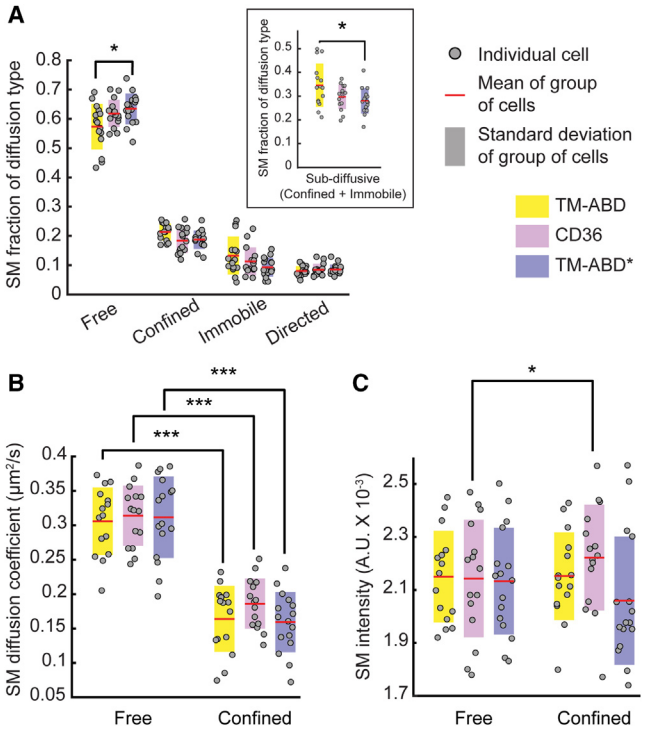

FIGURE 2 Dynamic organization of PM proteins reflects their actin binding ability. (*A–C*) Fraction (*A*), diffusion coefficient (*B*), and intensity (*C*) of SM tracklets of CD36 (*magenta*), TM-ABD (*yellow*), and TM-ABD* (*blue*) undergoing the indicated diffusion types. Inset in (*A*): fraction of sub-diffusive SM tracklets, i.e., confined and immobile combined. Gray circles show individual cell measurements (fraction in *A* and average in *B* and *C*). Red lines and shaded bars show mean and standard deviation, respectively, over group of cells representing a particular PM protein. Different PM proteins were compared using analysis of variance followed by Tukey-Kramer post-hoc analysis; free and confined properties for the same PM protein were compared using paired *t*-tests. $*p \leq 0.05$ and $***p \leq 0.001$. *p* values > 0.05 are not explicitly indicated. See Table S8 for sample size and other data set details. To see this figure in color, go online.

needed for SMI (roughly ∼20–30% of CD36 was labeled in our experiments) (58). The unique trend exhibited by CD36 (vis-a-vis TM-ABD and TM-ABD*) reflects the functional significance of CD36 clustering, in that clustering enhances CD36-downstream adaptor interactions, which could lead to confinement (5,50).

PM proteins of different diffusion types are associated with different local CA dynamics

Using the CA speckles that were matched to SM tracklets of CD36, TM-ABD, and TM-ABD* (Figs. 1 *E* and 3 *A*), we investigated the local speckle properties around the different PM proteins. While local speckle density (Fig. 3 *B*) and intensity (Fig. 3 *C*) were not different between different PM proteins and diffusion types, local speckle displacement magnitude was (unexpectedly) significantly higher for confined SM tracklets than for free tracklets (Fig. 3 *D*). Note that the corresponding cell-wide ("global") speckle properties did not differ between the cells expressing the different proteins (Fig. S4). The difference in local speckle displacement was largest and most significant for TM-ABD and weakest for TM-ABD*, with CD36 exhibiting intermediate behavior. The agreement between the strength of this local CA speckle phenotype and the extent of the PM protein's binding to actin (TM-ABD > CD36 > TM-ABD*) lends confidence in the SMI-FSM experimental and analysis pipeline.

As speckle displacement represents network remodeling (56,57), these observations indicate that free/confined PM proteins are associated with regions of lower/higher CA network remodeling. The weak but still significant difference in CA environment between free and confined TM-ABD* tracklets suggests that TM-ABD*, although unable to bind actin directly, is still influenced by CA, as observed previously (59). This could be either via nonspecific (steric) contacts of its intracellular domain with actin, or through the influence of CA on the PM as a whole by virtue of the many PM constituents that themselves interact with actin, or both (15,21).

PM protein mobility-CA relationships vary by CA density and PM protein diffusion type

To more closely inspect the relationship between PM protein behavior and the local CA environment at the SM level, we sought to quantify the (mathematical) dependence of SM tracklet properties (e.g., diffusion coefficient or intensity) on speckle properties through linear MVRG. MVRG would allow us to model the *collective* relationship between multiple CA speckle properties and SM diffusion coefficient or intensity. We utilized linear MVRG as the simplest model to quantify the coupling and characterize the relationship, if any, between these SM tracklet properties and speckle properties.

As a first step, and particularly to verify the validity of a potential linear relationship as modeled by MVRG, we made pairwise scatterplots of SM diffusion coefficient or SM intensity versus various CA speckle properties (separately for free and confined SM tracklets) on an individual cell basis (Fig. S5). The large data scatter in these scatterplots highlights the need for sensitive and rigorous statistical analysis tools, such as MVRG, to extract any potential relationships between the SM tracklet and speckle properties. As required for MVRG analysis, most scatterplots appeared linear. Note that "no relationship" is a special case of a linear relationship, with a regression coefficient (i.e., slope) of 0 (as will be tested in the ensuing analyses). An exception was the scatterplot of SM diffusion coefficient versus local CA speckle density, which exhibited an inverted v-shape in most cells (70% for CD36 and TM-ABD and 63% for TM-ABD* through objective assessment) (Note S6; Fig. S6, *A* and *B*). No other tested SM property-speckle property scatterplots exhibited an inverted v-shape: for example, for SM

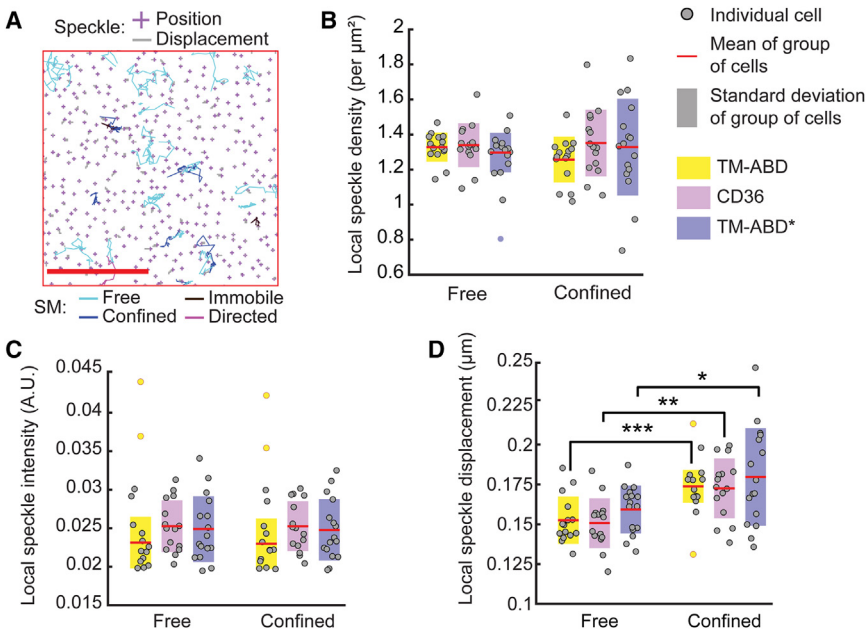

FIGURE 3 Local CA dynamics vary by PM protein diffusion type. (*A*) CD36 tracklets in one FSM interval overlaid on CA speckle positions at the beginning of that interval. Scale bar, 5 μm. (*B–D*) Density (*B*), intensity (*C*), and displacement magnitude (*D*) of speckles matched to SM tracklets of CD36 (*magenta*), TM-ABD (*yellow*), and TM-ABD* (*blue*) undergoing indicated diffusion types. Colors, circles, red lines, shaded bars, and statistical tests as in Fig. 2. (*D*) $^{**}p \leq 0.01$. Non-gray circles in (*C* and *D*) indicate outliers. See Table S8 for sample size and other data set details. To see this figure in color, go online.

diffusion coefficient versus local speckle displacement magnitude (Fig. S5 *B*), scatterplots were deemed to exhibit an inverted v-shape in <7% of cells.

Automatic estimation of the threshold at which the SM diffusion coefficient versus local CA speckle density scatterplot switched from positive to negative slope (Note S6) showed that it was similar between all cells and conditions, and was very close to the overall (global) speckle density in the imaged cells (1.18 vs. 1.25 speckles/μm^2; Figs. S6 *C* and S4 *A*). The inverted v-shape scatterplot between SM diffusion coefficient and local speckle density may be reflective of differential influence of CA on PM protein mobility at different CA density levels; the negative slope at higher densities is consistent with CA acting as a barrier to PM protein diffusion (15,21–23), while the positive slope at lower densities could reflect a role for CA in aiding PM protein movement (24,60). However, the inverted v-shape could also be a consequence of the discrete nature of speckles and spatial sampling by SM tracklets of different diffusivity (Note S7), especially as the optimal threshold at which the slope switches from positive to negative was found to be very close to the overall speckle density. Further investigations are needed to distinguish between these two possibilities, and none of our later results depend on either interpretation. Nevertheless, to satisfy the assumption of linearity in MVRG, we subdivided SM tracklets based on their local speckle density level: low density/sparse (local speckle density $<$ global density) and high density/dense (local speckle density $\geq$ global density). This yielded four subgroups of SM tracklets for MVRG analysis based on the combination of diffusion type (free versus confined) and local speckle density level (sparse versus dense) (Fig. S6 *D*).

MVRG of SM tracklet diffusion coefficient on various CA speckle properties (local displacement magnitude, density, and intensity) yielded significant MVRG coefficients for only speckle displacement magnitude and density (Figs. 4 and S7 *A*). The two speckle properties exhibited very little multicollinearity (variance inflation factor $\leq$ 1.96 for 97.8% of analyzed cells), allowing us to use them as independent predictors (in the mathematical/statistical sense) of SM tracklet diffusion coefficient (43). The MVRG coefficients with respect to local speckle density reflected the inverted v-shape scatterplot discussed above. The MVRG coefficients with respect to local speckle displacement magnitude were negative for all SM subgroups, thus indicating a negative relationship between PM protein diffusion and CA remodeling. This relationship was consistent with our earlier observation that freely diffusing/confined tracklets (i.e., higher/lower mobility) were associated with regions of lower/higher CA network remodeling (Fig. 3 *D*).

Comparison of the MVRG analysis results between the three model proteins provided further validation of SMI-FSM. Specifically, over the four subgroups, the actin binding control, TM-ABD, showed the strongest relationships with CA (i.e., most significant regression coefficients), the actin nonbinding control, TM-ABD*, showed the weakest relationships, and CD36 was in between. Here, as in the context of Fig. 3 *D*, the weaker but still significant relationships for TM-ABD* reflect the indirect influence of CA on TM-ABD* (59). Importantly, the agreement between the strength of the relationships identified by MVRG analysis and the actin binding ability/strength of the three PM proteins demonstrates the ability of SMI-FSM to meaningfully quantify CA-PM protein interplay. In Note S8, we present

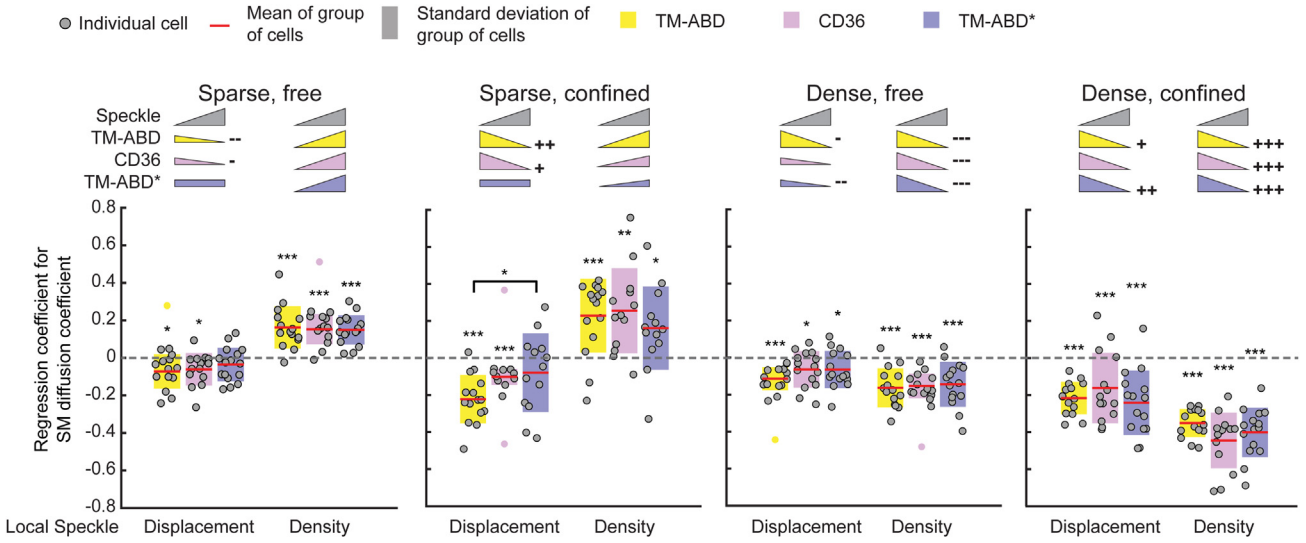

FIGURE 4 MVRG analysis reveals multiple regimes of PM protein-CA relationships. Coefficients from MVRG of SM diffusion coefficient on indicated local speckle properties, for CD36 (*magenta*), TM-ABD (*yellow*), and TM-ABD* (*blue*). MVRG analysis was performed separately for the four indicated subgroups of SM tracklets based on diffusion type and local speckle density pairings. Colors, circles, red lines, and shaded bars as in Figs. 2 and 3. MVRG coefficients significantly different from zero (*dashed gray line*), tested by *t*-test, are indicated by *, **, and *** above the MVRG coefficient plots for $p \leq 0.05$, 0.01, and 0.001, respectively. Differences between the MVRG coefficients of different PM proteins, tested by analysis of variance followed by Tukey-Kramer post-hoc analysis, are indicated by * above bracket for $p \leq 0.05$. Inset pictograms: visual summary of MVRG results. Triangle slope and direction represent significance and sign (positive or negative) of MVRG coefficient; rectangles indicate nonsignificant MVRG coefficients. Next to the triangles, +, ++, +++/−, −−, −−− indicate significant differences (greater/smaller) between free and confined MVRG coefficient magnitudes at the same density level (e.g., sparse free versus sparse confined) for each PM protein, tested by paired *t*-test, for $p \leq 0.05$, 0.01, and 0.001, respectively. In all tests, p values > 0.05 are not explicitly indicated. See Table S8 for sample size and other data set details. To see this figure in color, go online.

MVRG analysis for PM protein intensity (proxy for clustering) (Fig. S7 *B*), to also demonstrate the versatility of SMI-FSM.

Beyond validation, MVRG analysis yielded the following insight into the relationships of CA properties with PM protein diffusion coefficient. 1) At either density level, confined tracklets showed overall stronger relationships with CA than free tracklets, especially for TM-ABD and CD36, suggesting that confined PM proteins are more strongly associated with CA than freely diffusing PM proteins. 2) Overall, free tracklets associated with low speckle density had the weakest relationships with CA, confined tracklets associated with high density had the strongest, while the other two subgroups were in between. 3) Interestingly, differences in CA-PM protein relationships between the three proteins were detected for the diffusion-type speckle density subgroups with weaker relationships. This suggests that regimes of weaker CA influence allow for differential regulation of PM protein mobility in a manner that reflects their actin binding ability/strength, in contrast to regimes of strong and ubiquitous CA influence (as is the case of confined tracklets associated with high speckle density, where all PM proteins exhibit the same relationship with CA). These results highlight the ability of SMI-FSM to reveal the quantitative relationships between CA and PM protein dynamics, and its sensitivity to identify differences between them that reflect their actin binding ability.

Different CA dynamics in distinct subcellular regions are predictive of CD36 mobility

With its high spatiotemporal resolution, SMI-FSM is uniquely positioned to study PM proteins and CA in settings involving actin-dependent dynamic processes (in which case actin perturbation would not be a viable experimental strategy, as it would interfere with the process of interest). To demonstrate this capability, we applied SMI-FSM to Halo-CD36-expressing TIME-mNGrActin cells in later stages of spreading on fibronectin (after 4 h of plating instead of 72 h) (61), where they exhibited notable edge-ruffling activity (Videos S6 and S7). Consistent with the higher activity of the actin cytoskeleton under these conditions (61,62), the global CA speckle displacement was higher in 4-h-plated cells than in 72-h-plated cells (Fig. 5 *A*). Speckle density was similar in the two conditions (Fig. 5 *B*).

Visual inspection of these videos suggested that CA speckles behaved differently closer to the edge of the cells than further away (Video S6). To quantify these differences, we divided the imaged area of each cell into "edge" and "center" regions ($<\sim$4 μm and $>\sim$4 μm, respectively, from the segmented cell edge; Fig. 5, *C* and *D*; Note S9). With this division, the edge region covered the lamellipodium and part of the lamella right behind the cell edge (63). We found that both global CA speckle density and displacement were significantly lower in the edge region

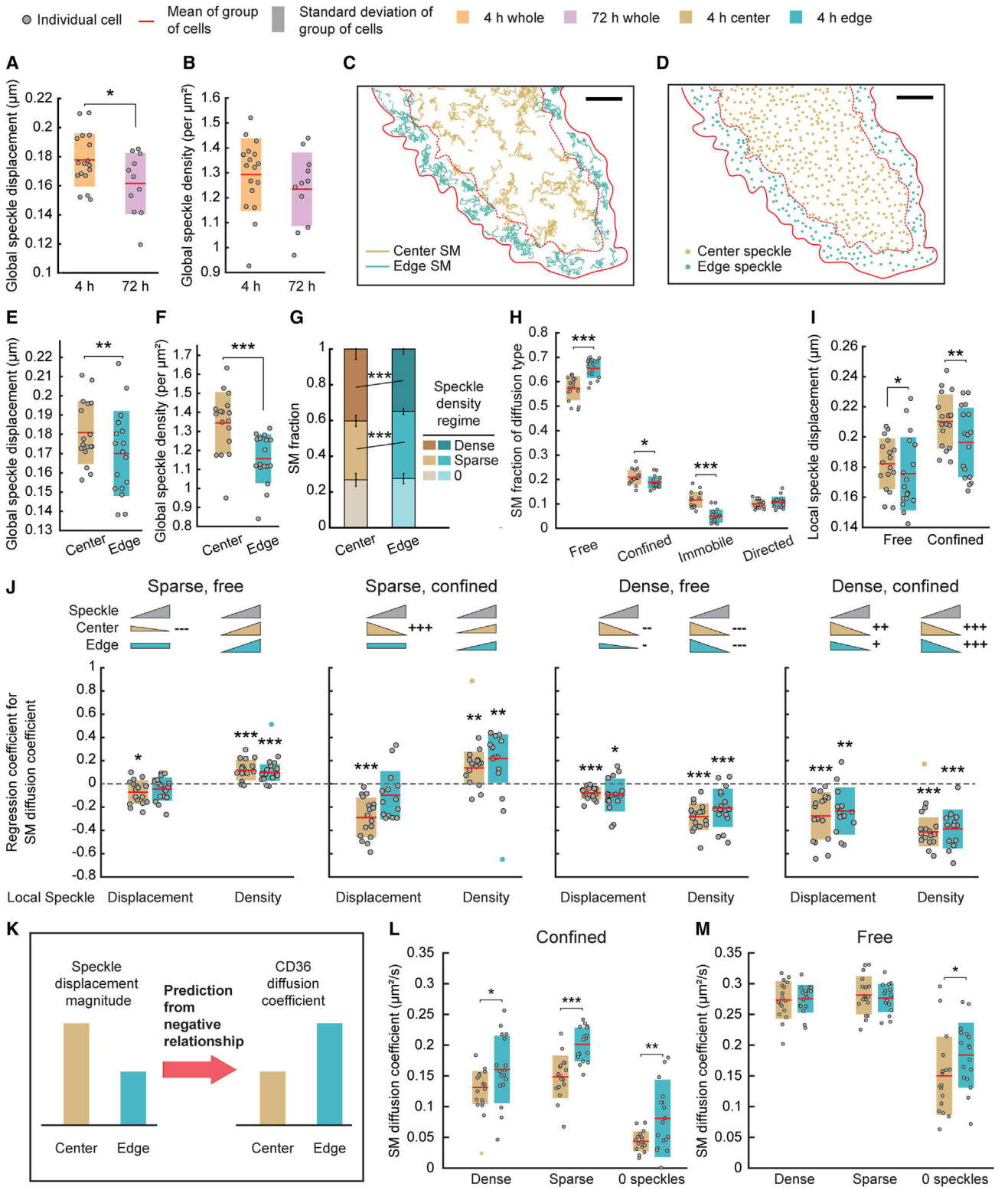

FIGURE 5 Differences in CD36 mobility between edge and center regions of ruffling cells correspond to differences in CA speckle dynamics. (*A* and *B*) Global speckle displacement magnitude (*A*) and density (B) of all CA speckles within the cell mask, in cells plated for 4 h (*orange*) or 72 h (*magenta*). Throughout this figure, circles, red lines, and shaded bars as in Figs. 2 and 3, unless indicated otherwise. (*C* and *D*) CD36 tracklets (*C*) and CA speckle detections (*D*) in one FSM interval, colored by their center (*brown*) or edge (*teal*) region classification. Solid and dashed red lines show, respectively, cell edge and boundary between cell center and edge regions. Scale bar, 5 μm. (*E* and *F*) Global speckle displacement magnitude (*E*) and density (*F*) of all CA speckles in center (*brown*) or edge (*teal*) regions. All following panels show analyses for center versus edge regions, using the same color coding.

(legend continued on next page)

than in the center region (Fig. 5, *E* and *F*). The lower CA speckle density in the edge region may be a consequence of membrane-CA detachment associated with cell edge protrusion (64,65).

With the lower density of CA in the edge region, the fraction of CD36 tracklets associated with sparse/dense CA was significantly higher/lower in the edge region versus in the center region (Fig. 5 *G*). Note that, in contrast to the lower density of CA in the edge region, the density of CD36 molecules was higher in the edge region than in the center region (Fig. S8). CD36 also exhibited a significantly higher fraction of freely diffusing tracklets in the edge region versus the center region (Fig. 5 *H*). In light of the lower CA speckle displacement at the edge (Fig. 5 *E*), this was consistent with our earlier observation that local speckle displacement magnitude was significantly lower for free SM tracklets than for confined tracklets (Fig. 3 *D*). This difference could also be related to the lower CA speckle density at the edge, given the generally observed diffusion barrier effect of CA (15,21–23), although our earlier analysis did not yield a difference in speckle density between free and confined tracklets (Fig. 3 *B*).

The difference in CA speckle displacement globally in the edge region versus the center region was reflected locally around the CD36 tracklets (Fig. 5 *I*). This provided us with a setting to test the coupling between CA dynamics and PM protein diffusion coefficient that SMI-FSM has revealed thus far. The MVRG relationships between CD36 diffusion coefficient and CA speckle properties were overall similar in the cells plated for 4 and 72 h (Fig. 5 *J* versus Fig. 4). The main exception was that the MVRG coefficient with respect to speckle displacement magnitude lost its significance in the edge region for SM tracklets at the sparse CA density level, suggesting some loss of coupling between CD36 diffusion and CA dynamics in the edge region of spreading cells. Nevertheless, considering the negative relationship between CA speckle displacement and SM tracklet diffusion coefficient that MVRG has revealed in the majority of analyzed conditions, we hypothesized that, given the lower speckle displacement in the edge region, the diffusion coefficient of CD36 tracklets will be correspondingly higher (Fig. 5 *K*). This was found to be indeed the case for confined tracklets, at all density levels (Fig. 5 *L*). The free tracklet behavior was less compliant with the MVRG rules, showing an edge versus center difference only for tracklets at extremely low CA density (0 speckles) (Fig. 5 *M*). The lack of difference for free tracklets at the other density levels most likely reflected 1) the overall weaker relationships of free tracklets to actin (Fig. 5 *J* and Fig. 4) and 2) the smaller difference in CA speckle displacement magnitude for free tracklets between edge and center regions (Fig. 5 *I*). Other cellular and molecular factors may be at play as well.

These experiments and analyses provide novel insight into the role of CA in the subcellular spatial modulation of CD36 mobility at the PM in the context of cell spreading and edge ruffling. Overall, SMI-FSM revealed reduced CA remodeling near the cell edge (reflected by smaller speckle displacements), which was largely predictive of increased mobility for CD36 in the same region. As CD36 mobility is related to its clustering, and clustering is in turn important for signaling (5,7,50), this modulation of CD36 mobility may lead to modulation of CD36 signaling in different subcellular regions (edge versus center) and in different cellular contexts (ruffling versus quiescent cells). The molecular underpinnings of the negative relationship between CA remodeling and CD36 mobility remain to be determined. Given that this relationship was also observed for TM-ABD and TM-ABD* (albeit to different degrees; Figs. 3 *D* and 4), the mechanisms underlying it are expected to pertain to the overall interplay between the PM and CA, and thus to affect most PM proteins.

SMI-FSM reveals heterogeneity and transients in CA and CD36 responses to actin perturbation

Cell-wide actin perturbation remains a commonly used approach to investigate the role of actin in regulating PM protein spatiotemporal organization, including our own previous work on CD36 (5,7). An inherent assumption in such approaches is that actin perturbation, and the corresponding PM protein modulation, are homogeneous throughout the cell. To test the validity of this assumption, we applied SMI-FSM to Halo-CD36-expressing TIME-mNGrActin cells exposed to Lat A. Lat A depolymerizes actin and causes severing of actin filaments (66). We initially treated TIME-mNGrActin cells with 200 nM Lat A, which led to fast, dramatic changes in the imaged CA network (and overall cell morphology). Within 2–4 min, stress fibers largely disappeared and actin node-like structures appeared (5,67) (Video S8). This was reflected as a large increase in CA speckle displacement, but with little change in speckle density (Fig. S9). The latter most likely reflected the CA

(*G*) Fraction of SM tracklets at different local speckle density levels. Each stacked bar represents the mean SM tracklet fraction over all cells. Error bar, corresponding standard deviation. (*H*) Fraction of CD36 SM tracklets undergoing indicated diffusion types. (*I*) Local speckle displacement magnitude for CA speckles associated with either free or confined CD36 tracklets. (*J*) Coefficients from MVRG of SM diffusion coefficient on local speckle displacement magnitude and density. MVRG analysis was performed separately for the indicated subgroups of SM tracklets based on subcellular region, diffusion type, and local speckle density. Dashed gray line and inset pictograms as in Fig. 4. (*K*) Schematic of prediction of CD36 diffusion coefficient given the difference in speckle displacement magnitude in center versus edge regions. (*L* and *M*) CD36 SM diffusion coefficient of confined (*L*) and free (*M*) SM tracklets at indicated CA speckle density levels. In (*A*) and (*B*), measurements were compared using two-sample *t*-test. In (*E*)–(*M*), measurements were compared between edge and center regions using paired *t*-test. $*p \leq 0.05$, $**p \leq 0.01$, $***p \leq 0.001$. p values > 0.05 are not explicitly indicated. See Table S8 for sample size and other data set details. To see this figure in color, go online.

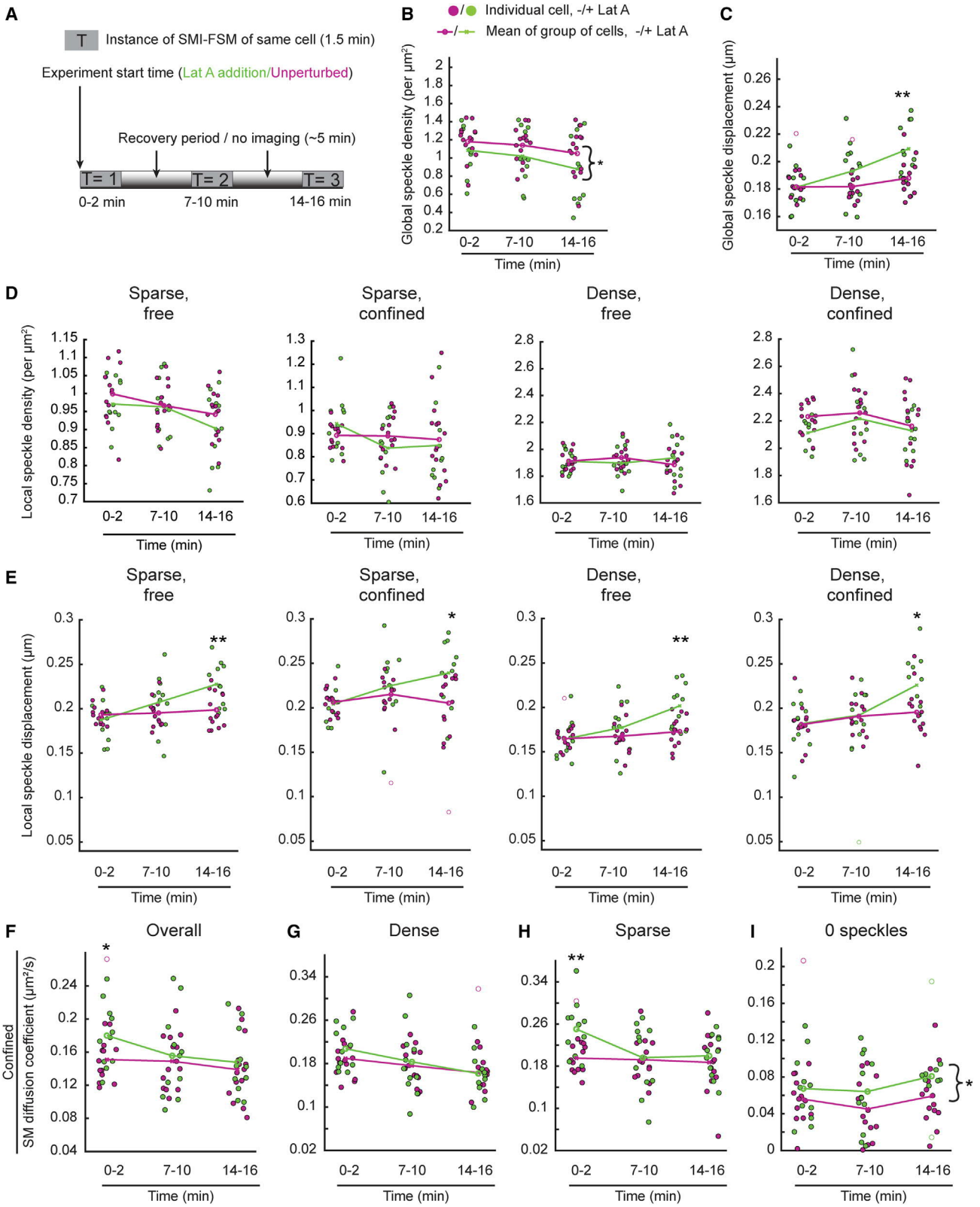

FIGURE 6 Latrunculin A treatment leads to heterogeneous changes in CA speckle properties and CD36 mobility. (*A*) Schematic of SMI-FSM at multiple instances of a single cell, with recovery periods in between, in the presence or absence of 30 nM Lat A. (*B* and *C*) Global speckle density (*B*) and global speckle displacement magnitude (*C*) of all CA speckles within the cell mask in the absence (*magenta*) or presence (*green*) of Lat A, at indicated instances. Filled circles, individual cell values from each instance. Unfilled circles with same outline color as filled circles indicate outliers. The means over the inlier

(legend continued on next page)

network adaptation and repolymerization (but with faster turnover) upon 200 nM Lat A treatment (52).

To minimize (or slow down) this adaptation, we treated the cells with 30 nM Lat A. Similarly low doses of Lat A (and the related Lat B) were used previously to perturb the actin network under various circumstances (68–70). At 30 nM, Lat A disrupted the actin network of TIME-mNGrActin cells gradually, reducing stress fibers and producing actin node-like structures over the course of 15–20 min (Fig. 6 *A*; Videos S9 and S10). It increased global CA speckle displacement and reduced global CA speckle density (Fig. 6, *B* and *C*). The decrease in speckle density is consistent with CA depolymerization. This suggests that there is less CA network adaptation and repolymerization at this low dose of Lat A, allowing us to dissect the effects of Lat A on CA and CD36, while reducing the complications of system adaptation over a longer period (15–20 min for 30 nM vs. 2–4 min for 200 nM).

First, we examined whether global changes in speckle properties upon Lat A treatment were reflected locally around CD36 molecules. We found that, while the distribution of CD36 molecules into high, low, and extremely low (0 speckles) CA density levels was slightly shifted because of the global reduction in CA speckle density (Fig. S10 *A*), the local speckle density around CD36 SM tracklets at the different CA density levels did not change (unlike the global trend) (Fig. 6 *D* versus *B*). Local speckle displacement followed the global trend, although with a delay around confined SM tracklets (Fig. 6 *E* versus *C*). These observations indicate that global changes in actin architecture and dynamics upon perturbation may not reflect the local CA changes sensed by specific PM proteins.

Second, we examined changes in CD36 mobility in response to Lat A treatment. We found that only the diffusion coefficient of confined SM tracklets was altered by Lat A treatment (Fig. 6, *F–I* and S10, *B*, *C*), in an intriguing CA density-dependent manner. Specifically, for tracklets associated with high local CA density, the diffusion coefficient was not different between Lat A-treated and untreated cells (Fig. 6 *G*). For those associated with low CA density, the diffusion coefficient was higher at 0–2 min after Lat A addition, but then similar in the absence or presence of Lat A at later times (Fig. 6 *H*). Interestingly, confined tracklets associated with extremely low CA density (0 speckles) showed a significant increase in their diffusion coefficient at all times after Lat A treatment (Fig. 6 *I*). As 30 nM Lat A reduced global speckle density (Fig. 6 *B*), we were concerned that the increase in diffusion coefficient for confined tracklets matched to 0 speckles could be due to the ability of SM tracklets to span a larger space without encountering any speckles. However, the span of confined tracklets matched to 0 speckles was similar in the absence and presence of Lat A (Fig. S10 *D*), thus eliminating this concern. These observations indicate that Lat A treatment increased CD36 tracklet mobility, as expected, but in a diffusion type-, CA density level-, and time-dependent manner.

It is interesting that the most sustained difference in the diffusion coefficient of confined tracklets between Lat A-treated and untreated cells was at extremely low CA density (0 speckles) (Fig. 6 *I*), where the influence of CA on CD36 is expected to be the most indirect. For these tracklets, the change in diffusion coefficient most likely reflects an overall modulation of PM organization upon actin perturbation, as inferred for the unrelated receptor EGFR (36). In contrast, for confined tracklets at the low and high CA density levels, which exhibited increasingly stronger relationships between CA and PM protein mobility (Fig. 4), the diffusion coefficient changed either transiently (sparse) or not at all (dense). Note that 200 nM Lat A treatment, which had a larger effect on CA speckle displacement, had an even weaker effect on CD36 mobility, except for possibly the diffusion coefficient of confined tracklets matched to 0 speckles (Fig. S9 *C*; compare with Fig. 6, *F* and *I*). These results, together with the observation that local CA changes around individual CD36 tracklets only partially followed the global CA changes, suggest spatial and temporal adaptation of the local CA environment and its relationship with CD36 to minimize the effect of actin perturbation on the system.

These analyses demonstrate the deep insight that SMI-FSM provides into the spatiotemporal co-organization of CA and PM proteins and its modulation upon cellular perturbation. The heterogeneity and transients in the response of CD36 to Lat A treatment are expected to be representative of the many PM proteins that are influenced by CA indirectly. More broadly, combining SMI-FSM with targeted molecular and cellular perturbations is expected to enable sensitive, "localized" (in space and time) analysis of the effect of these perturbations, thus providing a new depth of understanding of PM protein-CA interplay.

CONCLUSIONS

We developed SMI-FSM, a multiscale imaging and computational analysis framework that probes the dynamic

cells belonging to each instance are connected with lines for visual aid. Measurements from –LatA and +LatA per instance were compared by two-sample *t*-test. Measurements from –LatA and +LatA across all instances were compared using a paired *t*-test (curly brackets). *$p \leq 0.05$, **$p \leq 0.01$. p values > 0.05 are not explicitly indicated. (*D* and *E*) Local speckle density (*D*) and local speckle displacement magnitude (*E*) associated with the indicated subgroups of CD36 SM tracklets based on diffusion type and local speckle density pairings at the indicated instances. (*F–I*) Diffusion coefficient of confined CD36 SM tracklets in the absence or presence of 30 nM Lat A at the indicated instances, as calculated for all confined tracklets ("overall") (*F*) and the subsets associated with high (*G*) or low (*H*) speckle densities or 0 speckles (*I*). Colors, circles, lines, and statistical tests as in (*B* and *C*). See Table S8 for sample size and other data set details. To see this figure in color, go online.

properties of both PM proteins and CA and quantifies their relationships in live single cells. SMI-FSM has enabled, for the first time to the best of our knowledge, the characterization of CA architecture and dynamics and their relationships to the spatiotemporal organization of PM proteins at high resolution. Given the widespread use of SMI to study PM constituents, we expect SMI-FSM to be widely applicable to quantitatively explore the influence of CA architecture and dynamics on different PM proteins. Different FSM acquisition frame rates or degrees of actin labeling (e.g., down to SM speckles (71)) would allow the probing of CA at different spatial and temporal scales, thus allowing in-depth study of the multifaceted influence of CA on PM protein organization (21,24). The multidimensional data set of PM protein and CA properties derived simultaneously from a single cell by SMI-FSM would enable the exploration of the relationships between these properties, in unperturbed cells as well as upon perturbation. The analysis strategies within SMI-FSM can be also expanded, based on the questions of interest. SMI-FSM will be particularly powerful to study PM-CA interplay in the context of conditions involving actin-dependent dynamic cellular process.

DATA AND CODE AVAILABILITY

The MATLAB code implementing the computational analysis pipeline of SMI-FSM is available on GitHub (https://github.com/kjaqaman/SMI-FSM).

SUPPORTING MATERIAL

Supporting material can be found online at https://doi.org/10.1016/j.bpj.2023.08.007.

AUTHOR CONTRIBUTIONS

A.D., H.-T.N., and K.J. designed the research. A.D., B.d.R.-A., and N.T. performed the experiments. H.-T.N., A.D., D.T., and K.J. contributed to software development. A.D. and H.-T.N. analyzed the data. A.D., H.-T.N., and K.J. wrote the manuscript with input from all authors.

ACKNOWLEDGMENTS

We thank the Danuser lab at UTSW for help with FSM and the Mayor lab at NCBS for providing the GFPTM-Ez-AFBD and GFPTM-Ez-AFBD* constructs. We thank Dr. Tieqiao Zhang for microscopy support. We also thank the UTSW BioHPC facility for providing high-performance computing systems. This work was supported by funding from the National Science Foundation [MCB-2114417 (K.J.)], the National Institutes of Health/National Institute of General Medical Sciences [R35 GM119619 (K.J.)], the UTSW Endowed Scholars Program (K.J.), the Canadian Institutes of Health Research [PS 165816 (N.T.)], the Natural Sciences and Engineering Research Council of Canada [NSERC RGPIN-2018-05783 (N.T.)], the UTD/UTSW Green Fellowship program (D.T.) and the UTSW SURF program (D.T.).

DECLARATION OF INTERESTS

The authors declare no competing interests.

SUPPORTING CITATIONS

Reference (72) appears in the supporting material.

REFERENCES

1. Sungkaworn, T., M. L. Jobin, …, D. Calebiro. 2017. Single-molecule imaging reveals receptor-G protein interactions at cell surface hot spots. *Nature.* 550:543–547. https://doi.org/10.1038/nature24264.

2. Jacobson, K., P. Liu, and B. C. Lagerholm. 2019. The Lateral Organization and Mobility of Plasma Membrane Components. *Cell.* 177:806–819. https://doi.org/10.1016/j.cell.2019.04.018.

3. Anton, S. E., C. Kayser, …, A. Bock. 2022. Receptor-associated independent cAMP nanodomains mediate spatiotemporal specificity of GPCR signaling. *Cell.* 185:1130–1142.e11. https://doi.org/10.1016/j.cell.2022.02.011.

4. Kusumi, A., T. K. Fujiwara, …, K. G. N. Suzuki. 2012. Dynamic organizing principles of the plasma membrane that regulate signal transduction: commemorating the fortieth anniversary of Singer and Nicolson's fluid-mosaic model. *Annu. Rev. Cell Dev. Biol.* 28:215–250. https://doi.org/10.1146/annurev-cellbio-100809-151736.

5. Githaka, J. M., A. R. Vega, …, N. Touret. 2016. Ligand-induced growth and compaction of CD36 nanoclusters enriched in Fyn induces Fyn signaling. *J. Cell Sci.* 129:4175–4189. https://doi.org/10.1242/jcs.188946.

6. Cambi, A., F. de Lange, …, C. G. Figdor. 2004. Microdomains of the C-type lectin DC-SIGN are portals for virus entry into dendritic cells. *J. Cell Biol.* 164:145–155. https://doi.org/10.1083/jcb.200306112.

7. Jaqaman, K., H. Kuwata, …, S. Grinstein. 2011. Cytoskeletal control of CD36 diffusion promotes its receptor and signaling function. *Cell.* 146:593–606. https://doi.org/10.1016/j.cell.2011.06.049.

8. Low-Nam, S. T., K. A. Lidke, …, D. S. Lidke. 2011. ErbB1 dimerization is promoted by domain co-confinement and stabilized by ligand binding. *Nat. Struct. Mol. Biol.* 18:1244–1249. https://doi.org/10.1038/nsmb.2135.

9. McCabe Pryor, M., M. P. Steinkamp, …, B. S. Wilson. 2015. Orchestration of ErbB3 signaling through heterointeractions and homointeractions. *Mol. Biol. Cell.* 26:4109–4123. https://doi.org/10.1091/mbc.E14-06-1114.

10. Kalappurakkal, J. M., A. A. Anilkumar, …, S. Mayor. 2019. Integrin Mechano-chemical Signaling Generates Plasma Membrane Nanodomains that Promote Cell Spreading. *Cell.* 177:1738–1756.e23. https://doi.org/10.1016/j.cell.2019.04.037.

11. Garcia-Parajo, M. F., A. Cambi, …, K. Jacobson. 2014. Nanoclustering as a dominant feature of plasma membrane organization. *J. Cell Sci.* 127 (Pt 23):4995–5005. https://doi.org/10.1242/jcs.146340.

12. Bag, N., A. Wagenknecht-Wiesner, …, B. A. Baird. 2021. Lipid-based and protein-based interactions synergize transmembrane signaling stimulated by antigen clustering of IgE receptors. *Proc. Natl. Acad. Sci. USA.* 118, e2026583118. https://doi.org/10.1073/pnas.2026583118.

13. Heit, B., H. Kim, …, S. Grinstein. 2013. Multimolecular signaling complexes enable Syk-mediated signaling of CD36 internalization. *Dev. Cell.* 24:372–383. https://doi.org/10.1016/j.devcel.2013.01.007.

14. Liu, P., X. Wang, …, N. L. Thompson. 2012. The formation and stability of DC-SIGN microdomains require its extracellular moiety. *Traffic.* 13:715–726. https://doi.org/10.1111/j.1600-0854.2012.01337.x.

15. Freeman, S. A., A. Vega, …, S. Grinstein. 2018. Transmembrane Pickets Connect Cyto- and Pericellular Skeletons Forming Barriers to Receptor Engagement. *Cell.* 172:305–317.e10. https://doi.org/10.1016/j.cell.2017.12.023.

16. Jaqaman, K., and S. Grinstein. 2012. Regulation from within: the cytoskeleton in transmembrane signaling. *Trends Cell Biol.* 22:515–526. https://doi.org/10.1016/j.tcb.2012.07.006.

17. Mattila, P. K., F. D. Batista, and B. Treanor. 2016. Dynamics of the actin cytoskeleton mediates receptor cross talk: An emerging concept in tuning receptor signaling. *J. Cell Biol.* 212:267–280. https://doi.org/10.1083/jcb.201504137.

18. Mylvaganam, S., M. Riedl, …, S. A. Freeman. 2020. Stabilization of Endothelial Receptor Arrays by a Polarized Spectrin Cytoskeleton Facilitates Rolling and Adhesion of Leukocytes. *Cell Rep.* 31, 107798. https://doi.org/10.1016/j.celrep.2020.107798.

19. Vogel, S. K., F. Greiss, …, P. Schwille. 2017. Control of lipid domain organization by a biomimetic contractile actomyosin cortex. *Elife.* 6, e24350. https://doi.org/10.7554/eLife.24350.

20. Liu, A. P., and D. A. Fletcher. 2006. Actin polymerization serves as a membrane domain switch in model lipid bilayers. *Biophys. J.* 91:4064–4070. https://doi.org/10.1529/biophysj.106.090852.

21. Fujiwara, T. K., K. Iwasawa, …, A. Kusumi. 2016. Confined diffusion of transmembrane proteins and lipids induced by the same actin meshwork lining the plasma membrane. *Mol. Biol. Cell.* 27:1101–1119. https://doi.org/10.1091/mbc.E15-04-0186.

22. Suzuki, K., K. Ritchie, …, A. Kusumi. 2005. Rapid hop diffusion of a G-protein-coupled receptor in the plasma membrane as revealed by single-molecule techniques. *Biophys. J.* 88:3659–3680. https://doi.org/10.1529/biophysj.104.048538.

23. Li, J. H., P. Santos-Otte, …, H. Ewers. 2020. Directed manipulation of membrane proteins by fluorescent magnetic nanoparticles. *Nat. Commun.* 11:4259. https://doi.org/10.1038/s41467-020-18087-3.

24. Gowrishankar, K., S. Ghosh, …, M. Rao. 2012. Active Remodeling of Cortical Actin Regulates Spatiotemporal Organization of Cell Surface Molecules. *Cell.* 149:1353–1367, <Go to ISI>://WOS:000305119600018.

25. Fritzsche, M., D. Li, …, C. Eggeling. 2017. Self-organizing actin patterns shape membrane architecture but not cell mechanics. *Nat. Commun.* 8, 14347. https://doi.org/10.1038/ncomms14347.

26. Shelby, S. A., S. L. Veatch, …, B. A. Baird. 2016. Functional nanoscale coupling of Lyn kinase with IgE-FcεRI is restricted by the actin cytoskeleton in early antigen-stimulated signaling. *Mol. Biol. Cell.* 27:3645–3658. https://doi.org/10.1091/mbc.E16-06-0425.

27. Raghupathy, R., A. A. Anilkumar, …, S. Mayor. 2015. Transbilayer lipid interactions mediate nanoclustering of lipid-anchored proteins. *Cell.* 161:581–594. https://doi.org/10.1016/j.cell.2015.03.048.

28. Goswami, D., K. Gowrishankar, …, S. Mayor. 2008. Nanoclusters of GPI-anchored proteins are formed by cortical actin-driven activity. *Cell.* 135:1085–1097. https://doi.org/10.1016/j.cell.2008.11.032.

29. Stuart, L. M., S. A. Bell, …, K. J. Moore. 2007. CD36 signals to the actin cytoskeleton and regulates microglial migration via a p130Cas complex. *J. Biol. Chem.* 282:27392–27401. https://doi.org/10.1074/jbc.M702887200.

30. Bhanja, A., I. Rey-Suarez, …, A. Upadhyaya. 2022. Bidirectional feedback between BCR signaling and actin cytoskeletal dynamics. *FEBS J.* 289:4430–4446. <Go to ISI>://WOS:000668359700001. https://doi.org/10.1111/febs.16074.

31. Chugh, P., and E. K. Paluch. 2018. The actin cortex at a glance. *J. Cell Sci.* 131:jcs186254. <Go to ISI>://WOS:000443435600001. https://doi.org/10.1242/jcs.186254.

32. Ganguly, S., T. J. Pucadyil, and A. Chattopadhyay. 2008. Actin cytoskeleton-dependent dynamics of the human serotonin1A receptor correlates with receptor signaling. *Biophys. J.* 95:451–463. https://doi.org/10.1529/biophysj.107.125732.

33. Treanor, B., D. Depoil, …, F. D. Batista. 2010. The membrane skeleton controls diffusion dynamics and signaling through the B cell receptor. *Immunity.* 32:187–199. https://doi.org/10.1016/j.immuni.2009.12.005.

34. Fujiwara, T., K. Ritchie, …, A. Kusumi. 2002. Phospholipids undergo hop diffusion in compartmentalized cell membrane. *J. Cell Biol.* 157:1071–1081. https://doi.org/10.1083/jcb.200202050.

35. Andrews, N. L., K. A. Lidke, …, D. S. Lidke. 2008. Actin restricts FcepsilonRI diffusion and facilitates antigen-induced receptor immobilization. *Nat. Cell Biol.* 10:955–963. https://doi.org/10.1038/ncb1755.

36. Sankaran, J., H. Balasubramanian, …, T. Wohland. 2021. Simultaneous spatiotemporal super-resolution and multi-parametric fluorescence microscopy. *Nat. Commun.* 12:1748. https://doi.org/10.1038/s41467-021-22002-9.

37. Danuser, G., and C. M. Waterman-Storer. 2006. Quantitative fluorescent speckle microscopy of cytoskeleton dynamics. *Annu. Rev. Biophys. Biomol. Struct.* 35:361–387. https://doi.org/10.1146/annurev.biophys.35.040405.102114.

38. Noh, J., T. Isogai, …, G. Danuser. 2022. Granger-causal inference of the lamellipodial actin regulator hierarchy by live cell imaging without perturbation. *Cell Syst.* 13:471–487.e8. https://doi.org/10.1016/j.cels.2022.05.003.

39. Grimm, J. B., B. P. English, …, L. D. Lavis. 2015. A general method to improve fluorophores for live-cell and single-molecule microscopy. *Nat. Methods.* 12:244–250. https://doi.org/10.1038/nmeth.3256.

40. Jaqaman, K., D. Loerke, …, G. Danuser. 2008. Robust single-particle tracking in live-cell time-lapse sequences. *Nat. Methods.* 5:695–702. https://doi.org/10.1038/nmeth.1237.

41. Aguet, F., C. N. Antonescu, …, G. Danuser. 2013. Advances in analysis of low signal-to-noise images link dynamin and AP2 to the functions of an endocytic checkpoint. *Dev. Cell.* 26:279–291. https://doi.org/10.1016/j.devcel.2013.06.019.

42. Mendoza, M. C., S. Besson, and G. Danuser. 2012. Quantitative fluorescent speckle microscopy (QFSM) to measure actin dynamics. *Curr. Protoc. Cytom.* Chapter 2:Unit2.18. https://doi.org/10.1002/0471142956.cy0218s62.

43. Belsley, D. A., E. Kuh, and R. E. Welsc. 1980. Regression Diagnostics : Identifying Influential Data and Sources of Collinearity. Wiley.

44. NIST/SEMATECH e-Handbook of Statistical Methods.

45. Chen, Q., S. Nag, and T. D. Pollard. 2012. Formins filter modified actin subunits during processive elongation. *J. Struct. Biol.* 177:32–39. https://doi.org/10.1016/j.jsb.2011.10.005.

46. Saha, S., I. H. Lee, …, S. Mayor. 2015. Diffusion of GPI-anchored proteins is influenced by the activity of dynamic cortical actin. *Mol. Biol. Cell.* 26:4033–4045. https://doi.org/10.1091/mbc.E15-06-0397.

47. Silverstein, R. L., and M. Febbraio. 2009. CD36, a scavenger receptor involved in immunity, metabolism, angiogenesis, and behavior. *Sci. Signal.* 2:re3. https://doi.org/10.1126/scisignal.272re3.

48. Wong, H. S., V. Jaumouillé, …, L. A. Robinson. 2016. Chemokine Signaling Enhances CD36 Responsiveness toward Oxidized Low-Density Lipoproteins and Accelerates Foam Cell Formation. *Cell Rep.* 14:2859–2871. https://doi.org/10.1016/j.celrep.2016.02.071.

49. Thorne, R. F., J. F. Marshall, …, G. F. Burns. 2000. The integrins alpha3beta1 and alpha6beta1 physically and functionally associate with CD36 in human melanoma cells. Requirement for the extracellular domain OF CD36. *J. Biol. Chem.* 275:35264–35275. https://doi.org/10.1074/jbc.M003969200.

50. Jiménez, B., O. V. Volpert, …, N. Bouck. 2000. Signals leading to apoptosis-dependent inhibition of neovascularization by thrombospondin-1. *Nat. Med.* 6:41–48. https://doi.org/10.1038/71517.

51. da Rocha-Azevedo, B., S. Lee, …, K. Jaqaman. 2020. Heterogeneity in VEGF Receptor-2 Mobility and Organization on the Endothelial Cell Surface Leads to Diverse Models of Activation by VEGF. *Cell Rep.* 32, 108187. https://doi.org/10.1016/j.celrep.2020.108187.

52. Ponti, A., P. Vallotton, …, G. Danuser. 2003. Computational analysis of F-actin turnover in cortical actin meshworks using fluorescent speckle microscopy. *Biophys. J.* 84:3336–3352. https://doi.org/10.1016/S0006-3495(03)70058-7.

53. Vega, A. R., S. A. Freeman, …, K. Jaqaman. 2018. Multistep Track Segmentation and Motion Classification for Transient Mobility Analysis. *Biophys. J.* 114:1018–1025. https://doi.org/10.1016/j.bpj.2018.01.012.

54. Lee, G., G. Leech, …, R. M. Robertson-Anderson. 2021. Active cytoskeletal composites display emergent tunable contractility and restructuring. *Soft Matter.* 17:10765–10776. https://doi.org/10.1039/d1sm01083b.

55. Lee, K., H. L. Elliott, …, G. Danuser. 2015. Functional hierarchy of redundant actin assembly factors revealed by fine-grained registration of intrinsic image fluctuations. *Cell Syst.* 1:37–50. https://doi.org/10.1016/j.cels.2015.07.001.

56. Vallotton, P., S. L. Gupton, …, G. Danuser. 2004. Simultaneous mapping of filamentous actin flow and turnover in migrating cells by quantitative fluorescent speckle microscopy. *Proc. Natl. Acad. Sci. USA.* 101:9660–9665. https://doi.org/10.1073/pnas.0300552101.

57. Miller, C. M., E. Korkmazhan, and A. R. Dunn. 2022. Extraction of accurate cytoskeletal actin velocity distributions from noisy measurements. *Nat. Commun.* 13:4749. https://doi.org/10.1038/s41467-022-31583-y.

58. de Oliveira, L. R., and K. Jaqaman. 2019. FISIK: Framework for the Inference of In Situ Interaction Kinetics from Single-Molecule Imaging Data. *Biophys. J.* 117:1012–1028. https://doi.org/10.1016/j.bpj.2019.07.050.

59. Manzo, C., T. S. van Zanten, …, M. F. Garcia-Parajo. 2014. PSF decomposition of nanoscopy images via Bayesian analysis unravels distinct molecular organization of the cell membrane. *Sci. Rep.* 4:4354. https://doi.org/10.1038/srep04354.

60. Ditlev, J. A., A. R. Vega, …, M. K. Rosen. 2019. A composition-dependent molecular clutch between T cell signaling condensates and actin. *Elife.* 8, e42695. https://doi.org/10.7554/eLife.42695.

61. Reinhart-King, C. A., M. Dembo, and D. A. Hammer. 2005. The Dynamics and Mechanics of Endothelial Cell Spreading. *Biophys. J.* 89:676–689. https://doi.org/10.1529/biophysj.104.054320.

62. Ryan, G. L., N. Watanabe, and D. Vavylonis. 2012. A review of models of fluctuating protrusion and retraction patterns at the leading edge of motile cells. *Cytoskeleton (Hoboken).* 69:195–206. https://doi.org/10.1002/cm.21017.

63. Delorme, V., M. Machacek, …, G. M. Bokoch. 2007. Cofilin Activity Downstream of Pak1 Regulates Cell Protrusion Efficiency by Organizing Lamellipodium and Lamella Actin Networks. *Dev. Cell.* 13:646–662. https://doi.org/10.1016/j.devcel.2007.08.011.

64. Bisaria, A., A. Hayer, …, T. Meyer. 2020. Membrane-proximal F-actin restricts local membrane protrusions and directs cell migration. *Science.* 368:1205–1210. https://doi.org/10.1126/science.aay7794.

65. Welf, E. S., C. E. Miles, …, G. Danuser. 2020. Actin-Membrane Release Initiates Cell Protrusions. *Dev. Cell.* 55:723–736.e8. https://doi.org/10.1016/j.devcel.2020.11.024.

66. Fujiwara, I., M. E. Zweifel, …, T. D. Pollard. 2018. Latrunculin A Accelerates Actin Filament Depolymerization in Addition to Sequestering Actin Monomers. *Curr. Biol.* 28:3183–3192.e2. https://doi.org/10.1016/j.cub.2018.07.082.

67. Luo, W., C. H. Yu, …, A. D. Bershadsky. 2013. Analysis of the local organization and dynamics of cellular actin networks. *J. Cell Biol.* 202:1057–1073. https://doi.org/10.1083/jcb.201210123.

68. Higashida, C., S. Suetsugu, …, N. Watanabe. 2008. G-actin regulates rapid induction of actin nucleation by mDia1 to restore cellular actin polymers. *J. Cell Sci.* 121 (Pt 20):3403–3412. https://doi.org/10.1242/jcs.030940.

69. Jalal, S., S. Shi, …, Y. H. Tee. 2019. Actin cytoskeleton self-organization in single epithelial cells and fibroblasts under isotropic confinement. *J. Cell Sci.* 132, jcs220780. https://doi.org/10.1242/jcs.220780.

70. Qin, Z., W. Xia, …, T. Quan. 2018. YAP/TAZ regulates TGF-β/Smad3 signaling by induction of Smad7 via AP-1 in human skin dermal fibroblasts. *Cell Commun. Signal.* 16:18. https://doi.org/10.1186/s12964-018-0232-3.

71. Yamashiro, S., H. Mizuno, …, N. Watanabe. 2014. New single-molecule speckle microscopy reveals modification of the retrograde actin flow by focal adhesions at nanometer scales. *Mol. Biol. Cell.* 25:1010–1024. https://doi.org/10.1091/mbc.E13-03-0162.

72. Köster, D. V., K. Husain, …, S. Mayor. 2016. Actomyosin dynamics drive local membrane component organization in an *in vitro* active composite layer. *Proc. Natl. Acad. Sci. USA.* 113:E1645–E1654. https://doi.org/10.1073/pnas.1514030113.